Trade Wind Cloud Evolution Observed by Polarization Radar: Relationship to Giant Condensation Nuclei Concentrations and Cloud Organization

HILARY A. MINOR,* ROBERT M. RAUBER, SABINE GÖKE,+ AND LARRY DI GIROLAMO

Department of Atmospheric Sciences, University of Illinois at Urbana–Champaign, Urbana, Illinois

(Manuscript received 17 September 2010, in final form 23 November 2010)

ABSTRACT

Shallow marine trade wind cumuli are one of the most prevalent cloud types in the tropical atmosphere. Understanding how precipitation forms within these clouds is necessary to advance our knowledge concerning their role in climate. This paper presents a statistical analysis of the characteristic heights and times at which precipitation in trade wind clouds passes through distinct stages in its evolution as defined by the equivalent radar reflectivity factor at horizontal polarization Z_H, the differential reflectivity Z_{DR}, and the spatial correlation between and averages of these variables. The data were obtained during the Rain in Cumulus over the Ocean (RICO) field campaign by the National Center for Atmospheric Research (NCAR) S-band dual-polarization (S-Pol) Doppler radar, the National Science Foundation (NSF)–NCAR C130 aircraft, and soundings launched near the radar. The data consisted of 76 trade cumuli that were tracked from early echo development through rainout on six days during RICO. Trade wind clouds used in the statistical analyses were segregated based on giant condensation nuclei (GCN) measurements made during low-level aircraft flight legs on the six days.

This study found that the rate of precipitation formation in shallow marine cumulus was unrelated to the GCN concentration in the ambient environment. Instead, the rate at which precipitation developed in the clouds appeared to be related to the mesoscale forcing as suggested by the cloud organization. Although GCN had no influence on the rate of precipitation development, the data suggest that they do contribute to a modification of the rain drop size distribution within the clouds. With very few exceptions, high threshold values of Z_{DR} were found well above cloud base on days with high GCN concentrations. On the days that were exceptions, these threshold values were almost always achieved near cloud base.

1. Introduction

Shallow marine trade wind cumuli are one of the most prevalent cloud types in the tropical atmosphere. Precipitation from shallow oceanic tropical convection is important because of its potential to impact marine boundary layer (MBL) dynamics and cloud organization (Rauber et al. 2007; Xue et al. 2008; Snodgrass et al. 2009), as well as its potential to modify aerosol distributions. Additionally, shallow tropical clouds can have direct and indirect climatic effects (Twomey 1974; Albrecht 1989; Pincus and Baker 1994) and regulate heat and moisture transported into the intertropical convergence zone, which influences the Hadley circulation (Betts 1997; Siebesma 1998; Stevens 2005). Excellent reviews of trade wind cumuli and their role in the global circulation are given by Betts (1997), Siebesma (1998), and Stevens (2005). Understanding how precipitation forms within shallow tropical convection and knowing the effects that precipitation has on trade wind cloud organization as well as the thermal, moisture, and aerosol properties of the MBL are necessary if we are to advance our knowledge concerning the role of these clouds in the climate system.

The tendency of shallow marine trade wind cumuli to readily form rain has motivated research into the mechanisms of rain formation in warm clouds for over a half century. Despite extensive research on warm rain formation, one of the classic unsolved problems in cloud physics is the explanation of the perceived short time between initial cloud formation and the onset of precipitation in warm

* Current affiliation: Sonoma Technology, Inc., Petaluma, California.

+ Current affiliation: Department of Physics, University of Helsinki, Helsinki, Finland.

Corresponding author address: Robert M. Rauber, Department of Atmospheric Sciences, University of Illinois at Urbana–Champaign, 105 S. Gregory St., Urbana, IL 61801.
E-mail: r-rauber@illinois.edu

DOI: 10.1175/2010JAS3675.1

TABLE 1. S-Pol radar characteristics during RICO.

Wavelength	10.62 cm
Receivers (2)	H and V simultaneously
Noise power	−115.5 dBm
Antenna	Parabolic, center feed
Beamwidth	0.91°
Scan rate	Up to 18° s^{-1} each axis, 30° s^{-1} with pulley change
Gate spacing	150 m
No. of samples	50 pulses per beam
Recorded variables	Doppler radial velocity V_R, radar reflectivity factor Z, differential radar reflectivity Z_{DR}
Lat	17.607 50°
Lon	−61.823 95°
Alt	7 m

clouds. A time interval of about 20 min is often quoted for initiation of warm rain; however, few field observations carefully define the starting time of trade wind cumuli development or rain initiation (Paluch and Knight 1986; Knight et al. 2002, 2008; Reiche and Lasher-Trapp 2010).

Many hypotheses have been proposed that attempt to account for the few larger cloud drops needed to initiate coalescence and subsequently produce rainfall in shallow, maritime cumuli. One of the simplest mechanisms used to explain the initiation of warm rain in trade wind cumuli is the presence of giant (sea salt) condensation nuclei (GCN) particles (dry radius $r > 1$ μm) in the marine atmosphere (e.g., Woodcock and Gifford 1949; Woodcock 1953; Ochs and Semonin 1979; Johnson 1982, 1993; Szumowski et al. 1999; Laird et al. 2000; Lasher-Trapp et al. 2001; Colón-Robles et al. 2006; Knight et al. 2002, 2008; Reiche and Lasher-Trapp 2010; Arthur et al. 2010). Soluble sea salts, when ingested into cloud base, can almost immediately begin to grow by collecting cloud drops and require little or no growth by condensation (Johnson 1979). If present in large enough concentrations, GCN can lead to the formation of large raindrops in 15–20 min (Szumowski et al. 1999).

Past polarization radar studies present evidence regarding the importance of GCN in the initiation of precipitation in small cumuli. Caylor and Illingworth (1987), Illingworth et al. (1987), and Illingworth (1988) used differential reflectivity measurements to show that low concentrations of large raindrops were present simultaneously with early weak radar reflectivity echoes in continental cumulus, supporting the hypothesis that early large raindrops form on GCN. Knight et al. (2002) confirmed these findings using dual-polarization measurements of early radar echoes from shallow cumuli in Florida. The early radar echoes in Florida had columns of high differential reflectivity that extended from near cloud top through cloud base as the early radar reflectivity developed near

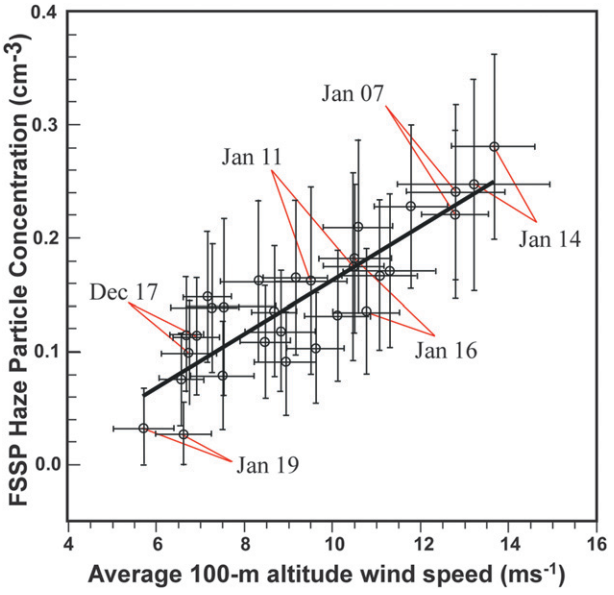

FIG. 1. Haze particle concentrations measured 100 m above the ocean surface with the Forward Scattering Spectrometer Probe (FSSP) in clear air regions as a function of wind speed. The circles denote mean values and the bars denote standard deviations. Data from two circles on the same day were taken 4 h apart. Adapted from Colón-Robles et al. (2006).

cloud top. In the middle to lower portions of the cloud, the differential reflectivity signal was characteristic of raindrops with diameters between 1 and 3 mm. More recent dual-polarization radar studies by Knight et al. (2008), Reiche and Lasher-Trapp (2010), and Arthur et al. (2010) using data from the Rain in Cumulus over the Ocean (RICO) experiment have found the importance of the giant aerosol to precipitation formation in small trade wind cumuli to be minor.

The dynamics of trade wind clouds can also be expected to influence the rate of precipitation formation. The updraft strength in the trade wind environment should be related to the mesoscale cloud organization [cf. Fig. 7 of Rauber et al. (2007) and Fig. 16 of Snodgrass et al. (2009)], as the forcing along the leading edge of a cold pool or outflow boundary would be more intense than the forcing associated with wind-parallel cloud streets. Indeed, Snodgrass et al. (2009; see their Fig. 14) showed the relationships between radar-estimated rainfall rate and the Multiangle Imaging Spectroradiometer (MISR) cloud-top height for all the RICO clouds observed simultaneously by MISR and the National Center for Atmospheric Research (NCAR) S-band dual-polarization (S-Pol) Doppler radar (thousands of clouds on 13 separate days). They showed that the average rainfall rate increases with cloud-top height over the altitude range of RICO clouds. They also examined collocated radar and MISR data (cf. Fig. 5 of Snodgrass et al. 2009), as well as collocated radar and

TABLE 2. Adapted from Colón-Robles et al. (2006): the mean wind speeds 100 m above the ocean surface and clear air FSSP haze particle concentrations (conc.) measured during 30-min-long circular flight patterns flown by the NCAR C130 4–5 h apart in the morning and afternoon.

Date	Morning conc. (cm^{-3})	Morning wind ($m\ s^{-1}$)	Afternoon conc. (cm^{-3})	Afternoon wind ($m\ s^{-1}$)
19 Jan 05	0.03 ±0.04	5.7 ±0.7	0.03 ±0.03	6.6 ±0.6
17 Dec 04	0.10 ±0.05	6.7 ±0.6	0.11 ±0.05	6.9 ±0.5
16 Jan 05	0.16 ±0.08	9.5 ±0.8	0.18 ±0.08	10.5 ±0.7
11 Jan 05	0.18 ±0.07	10.5 ±0.8	0.14 ±0.05	10.8 ±0.8
7 Jan 05	0.22 ±0.07	12.8 ±0.8	0.24 ±0.08	12.8 ±1.0
14 Jan 05	0.25 ±0.09	13.2 ±1.7	0.28 ±0.08	13.2 ±1.0

visible Geostationary Operational Environmental Satellite (GOES) imagery over the entire 62 days of radar operation. They concluded that the cloud organization on the mesoscale was clearly related to precipitation intensity and distribution. Specifically, they found that very little of the total rainfall was associated with clouds organized into wind-parallel streets and nearly all the rainfall came from cumulus clusters aligned in arc-shaped formations associated with cold-pool outflows.

The importance of microphysical processes compared to dynamic forcing in rain formation has not been investigated in the trade wind environment. This paper examines the statistical behavior of precipitation evolution of trade wind cumulus clouds, with a focus on determining the characteristic heights and times at which precipitation passes through distinct stages in its evolution as defined by the equivalent radar reflectivity factor at horizontal polarization Z_H and the differential reflectivity Z_{DR}. In the statistical approach, we introduce the spatial correlation coefficient between Z_H and Z_{DR} as a variable that permits a better understanding of the relationship between the position of large raindrops and the bulk of the rainfall in a cloud. We use the results from the statistical analysis to examine the relationship among the precipitation evolution, the GCN concentration, and mesoscale cloud organization, and we evaluate whether microphysical processes are sufficient to trigger precipitation independent of the type of dynamic forcing occurring in the marine trade wind environment.

2. Analysis procedures

RICO took place over the western tropical Atlantic off the Caribbean island of Barbuda between November 2004 and January 2005. Rauber et al. (2007), Snodgrass et al. (2009), and Nuijens et al. (2009) describe the weather conditions over this region during this time period. Clouds observed during RICO were located over the open Atlantic and had tops below the freezing level.

The NCAR S-band (10 cm) dual-polarization Doppler radar was located on Barbuda. Characteristics of the radar during RICO are given in Table 1. The scanning strategy was designed to capture the complete life cycle of a cloud at high temporal resolution as the cloud progressed across the radar domain. The radar scanned constant-elevation angle sweeps across 180° sectors with the mid-angle of the sector aligned normal to the prevailing cloud motion. Volume scans typically had 9–10 constant-elevation angle sweeps at angles ranging from 0.5° to 16.8°. A volume scan took 3–4 min to complete. Every 20 min, the lowest elevation (0.5°) of the volume scans swept 360° (rather than 180°) as part of routine surveillance. Variables used in this paper include Z_H, Z_{DR}, and the radial velocity V_R.

The S-Pol radar observations offered nearly continual coverage over the lifetime of small cumulus and therefore

TABLE 3. Thermodynamic and weather characteristics for the six analysis days.

Date	Time (UTC)	T_{LCL} (°C)	H_{LCL} (m)	P_{LCL} (hPa)	Wind direction (°) at LCL	TMBL height (hPa)	CAPE ($J\ kg^{-1}$)	Area avg rain rate ($mm\ day^{-1}$)
17 Dec 04	0754:58	22.63	289.29	979.40	79	720	2545	0.9
17 Dec 04	1349:45	19.80	709.29	936.09	75	785	1064	
17 Dec 04	1655:02	20.01	716.62	934.40	74	880	1811	
17 Dec 04	1953:38	21.32	579.82	948.61	80	800	1717	
11 Jan 05	1059:55	20.43	417.49	968.41	71	590	962	2.1
11 Jan 05	1658:33	18.81	782.41	929.23	85	605	936	
14 Jan 05	1045:15	20.54	502.71	960.24	79	760	1636	2.8
14 Jan 05	1718:02	17.92	774.34	930.47	90	690	744	
19 Jan 05	1050:29	21.36	362.07	971.48	23	630	1209	1.8
19 Jan 05	1808:03	18.83	559.91	949.11	13	610	317	
7 Jan 05	1055:56	20.43	564.14	953.59	63	630	1008	0.9
7 Jan 05	1701:54	19.46	672.58	941.92	70	740	1229	
7 Jan 05	2255:40	20.97	522.57	959.15	65	600	1055	
16 Jan 05	1103:21	20.22	519.73	955.65	83	550	1096	1.8
16 Jan 05	1807:28	17.73	836.56	920.69	100	580	270	

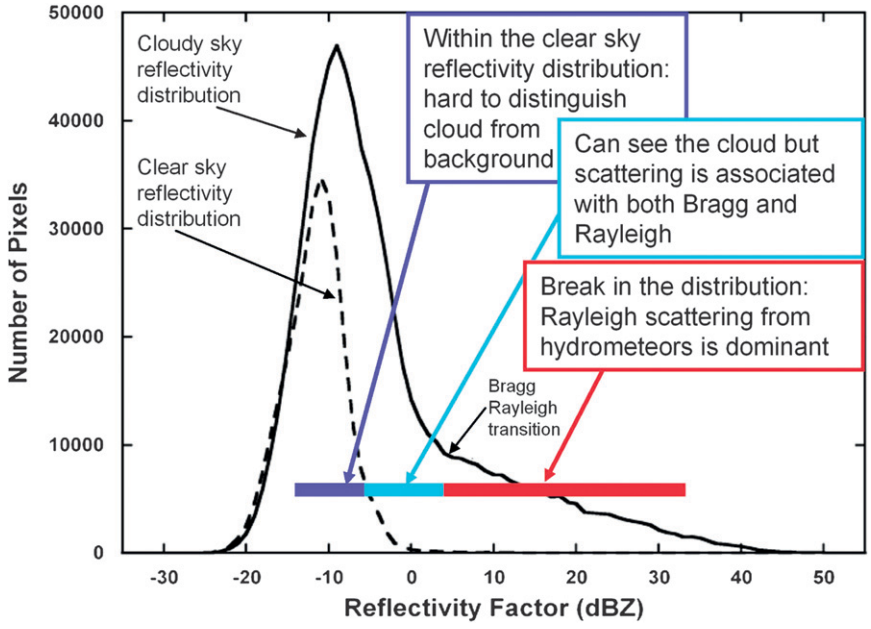

FIG. 2. Cloudy and clear sky reflectivity distributions as a function of radar reflectivity determined from collocated radar and satellite data from RICO. Adapted from Snodgrass et al. (2009).

had the ability to capture the very elusive first appearances of both cloud formation and precipitation initiation. Additionally, the polarimetric radar measurements provided indirect information on droplet size and drop number concentration. The equivalent radar reflectivity factor at horizontal polarization is proportional to the drop number concentration and sixth power of the drop diameter and is useful in estimating the size and number concentration of the drops, whereas differential reflectivity, the ratio of the horizontally polarized reflectivity to the vertically polarized reflectivity, gives an estimate of the mean raindrop size. Perfectly spherical drops produce Z_{DR} values of 0 dB (equal horizontal and vertical dimensions), while larger drops (diameter >1 mm) that have been flattened through aerodynamic forcing (larger horizontal cross section than vertical cross section) have Z_{DR} values greater than 0 dB (Caylor and Illingworth 1987; Knight et al. 2002). Identification of high Z_{DR} values ($\sim$>1 dB) with low Z_H ($\sim$<10 dBZ) are indicative of a few large droplets developing in the absence of large concentrations of other raindrops. High Z_H values (>10 dBZ) with low Z_{DR} ($\sim$<1 dB) indicate the opposite.

The National Science Foundation (NSF)–NCAR C130 aircraft operated over the Atlantic east of Barbuda and sampled the same cloud field observed by the radar (Rauber et al. 2007). Giant particle concentrations (diameter range 3.1–46.5 μm), most likely deliquesced seasalt aerosol, were measured at the beginning and end of each flight during 60-km-diameter circles flown 100 m above the ocean surface (Colón-Robles et al. 2006). Radar data from six flight days, chosen to represent the full range of giant particle concentrations observed during RICO, were used in this research (Fig. 1; Table 2).

Table 3 summarizes the thermodynamic and weather characteristics of these six days. Some of the data in Table 3 were derived from soundings, which were launched 2–4 times per day from the southeastern tip of Barbuda. The average daily rain rates were from Snodgrass et al. (2009). Cloud-base temperature, pressure, and height were estimated using sounding data closest to the radar time. The pressure, temperature, and dewpoint temperature near the 50-m level, an empirical formula for the temperature of cloud base (Inman 1969), the dry adiabatic lapse rate, and the hydrostatic equation were used to calculate these variables using the same procedure as Laird et al. (2000). Average cloud base was 587 m, with a standard deviation

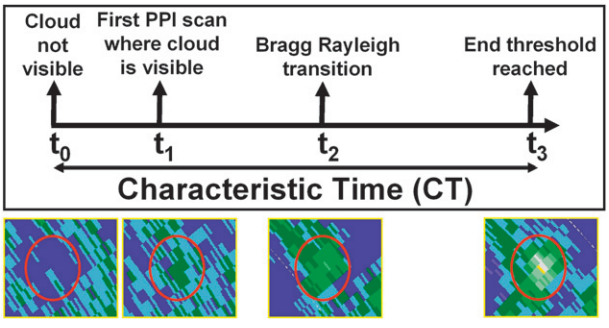

FIG. 3. Definition of characteristic time with radar reflectivity images corresponding to the different stages of cloud development.

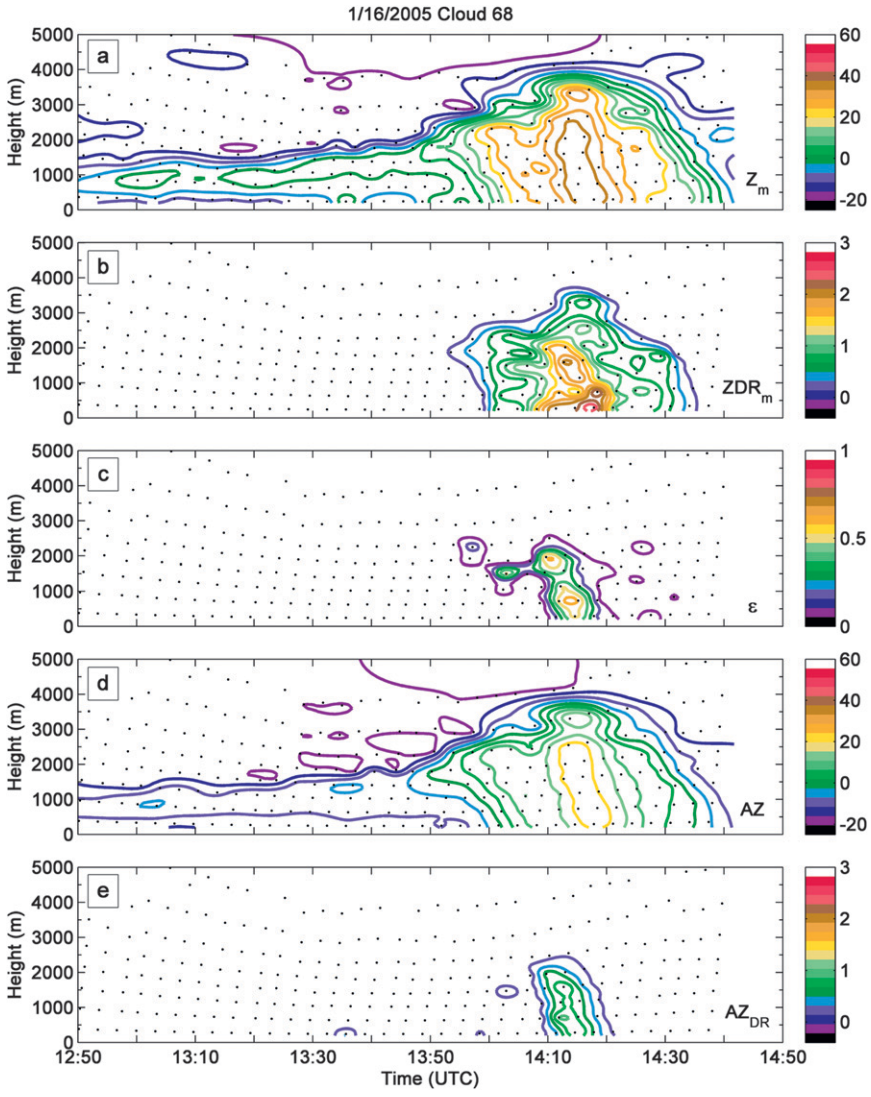

FIG. 4. Time–height cross section showing the temporal and spatial evolution of (a) Z_m, (b) ZDR_m, (c) ε, (d) AZ, and (e) AZ_{DR} of cloud 68 on 16 Jan 2005. The black dots in (a) and (b) are plotted at the exact time and location where Z_m and ZDR_m occurred on each slice. The black dots in (c)–(e) represent the mid-time of each slice for which ε, AZ, and AZ_{DR} were calculated. The contours in all panels were developed after the irregular data were interpolated to a Cartesian grid with spacing of 25 s on the abscissa and 100 m on the ordinate. Only values of $ZDR_m > 0$, $\varepsilon > 0$, and $AZ_{DR} > 0$ are plotted. The contours in (a) and (d) begin at −25 dBZ and are spaced at 5-dBZ intervals. The contours in (b) and (e) begin at 0.2 dB and are spaced at 0.2-dB intervals. The contours in (c) begin at 0.1 and are spaced at 0.1 intervals. The left side of the diagram corresponds to the time t_1 in Fig. 3.

of 160 m and extreme values of 836 and 289 m. The top of the marine boundary layer (TMBL), defined as the altitude that marked a substantial reduction in relative humidity, varied from 880 to 550 hPa. An inversion was not always coincident or even present at the top of the TMBL (Rauber et al. 2007). The CAPE values were typical of the tropics [~(1000–2500) J kg^{-1}] except in the cases when a sufficiently strong tropical inversion was present (~300 J kg^{-1}), which inhibited a lifted parcel from rising to the tropopause. However, deep convection was not present anywhere near the study area on any of the days.

Individual clouds were selected for analysis based on the following five criteria: 1) the cloud could be tracked backward in time until the echo disappeared into the noise background, 2) the cloud had to form within 60 km of the radar and at closest approach the cloud had to be at least 10 km away from the radar, 3) Z_H within the cloud had to reach at least 15 dBZ, 4) the cloud had to remain

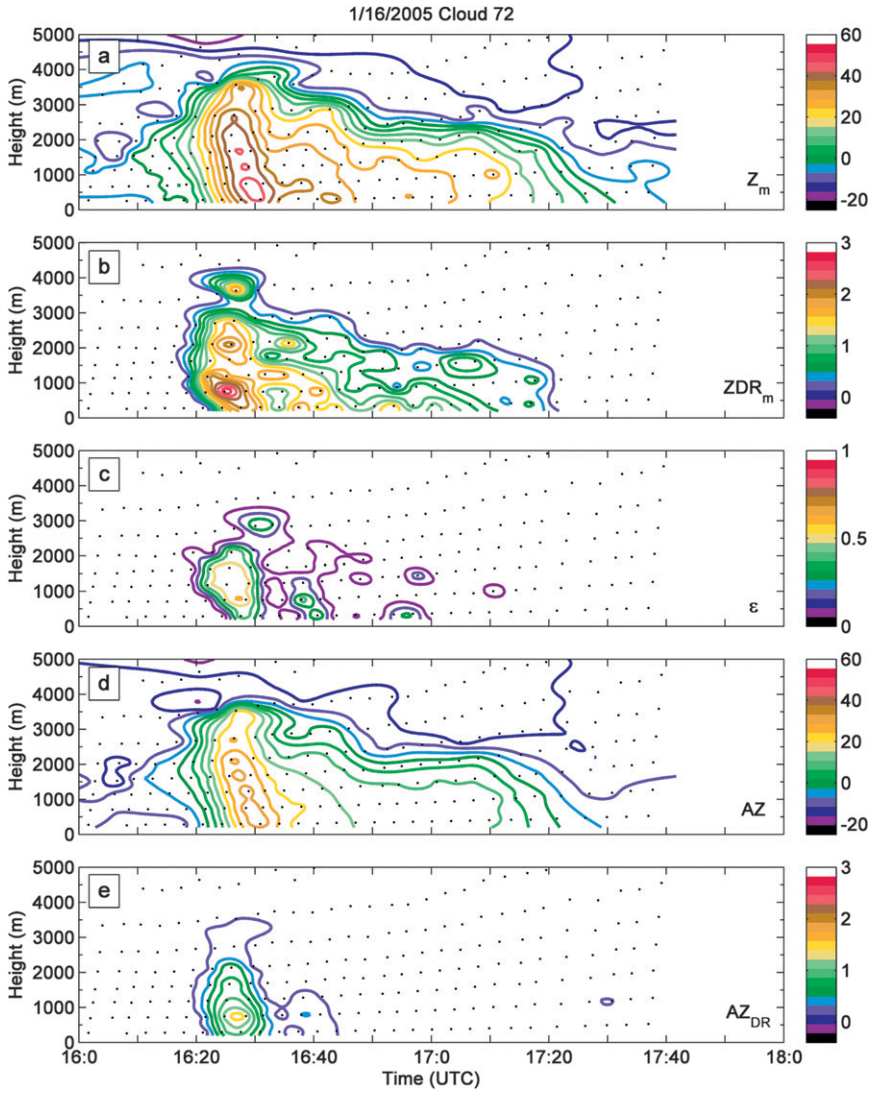

FIG. 5. As in Fig. 4, but for cloud 72 on 16 Jan 2005.

isolated from other cloud echoes from its first appearance until it achieved threshold values of Z_H as defined below, and 5) achievement of all threshold values had to occur within 60 km of the radar. It was extremely difficult to find clouds that satisfied these strict criteria. All clouds that met these criteria on each analysis day were tracked until they disappeared into the noise background, grew into larger systems, lost individual identity, or moved beyond 60 km. In our search for these clouds every radar sweep for the period from ~2 h before to ~2 h after the flight was visually examined and every cloud that met the criteria was used. In all, 76 clouds over six days were identified that met these criteria. The date, time, range, azimuth, and elevation that each cloud first crossed the 10-dBZ Z_H threshold are tabulated in the appendix. The full volume radar data encompassing each cloud were extracted for further processing, and the remaining data outside the cloud were discarded. For convenience, we will refer to the part of a single elevation sweep file containing the cloud as a *slice*.

Sea clutter was not a problem because the radar site was chosen such that a direct path from the antenna to the sea was blocked by a 10-m-high ridge on the eastern side of Barbuda. However, nonmeteorological echoes, primarily due to frigate birds (*Fregata magnificens*), were a common occurrence. These birds, which have a 2-m wing span and are capable of flying to altitudes of 2500 m, produced Z_{DR} signatures that ranged from greater than 4 dB to below −2 dB depending on their horizontal or vertical tilt. The birds produced a wide range of V_R signatures that varied depending on whether they flew actively or passively, and along or across the beam. The birds sometimes produced anomalous echoes when they used the early cloud

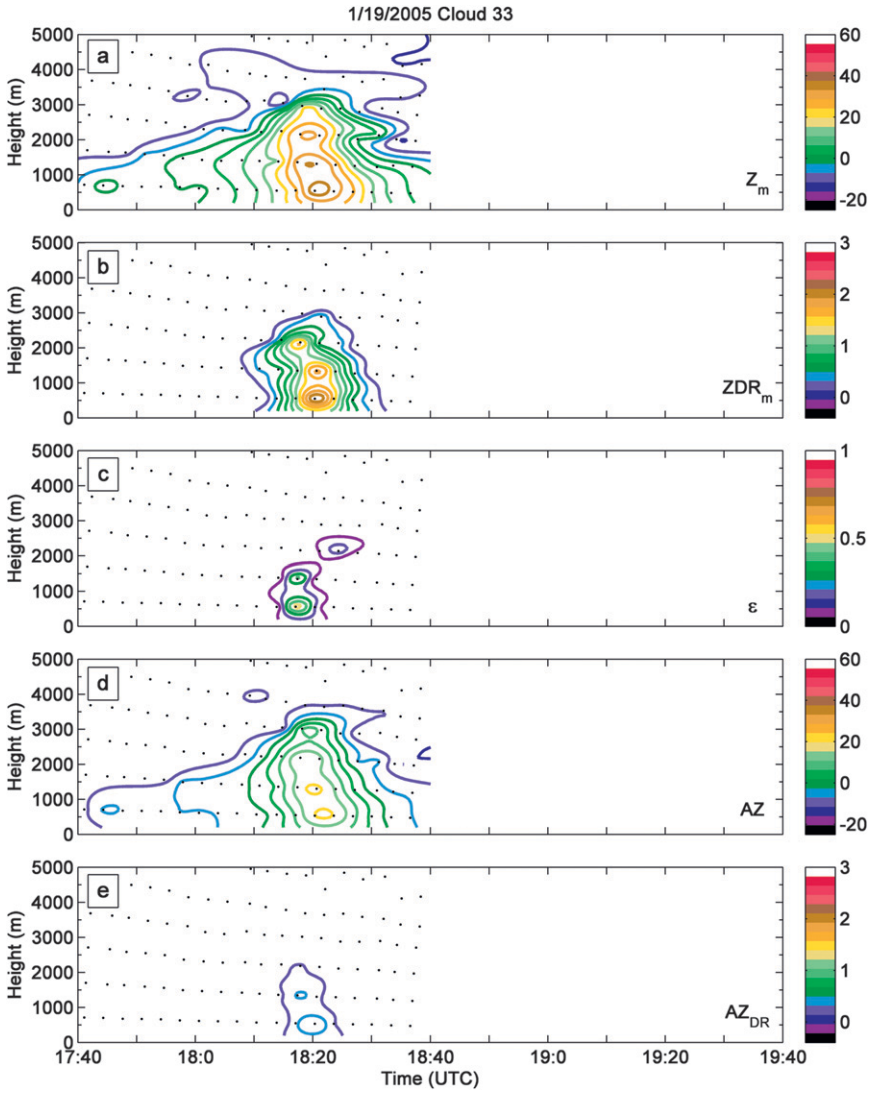

FIG. 6. As in Fig. 4, but for cloud 33 on 19 Jan 2005.

updraft to soar, although bird echoes were much less common once rain developed, suggesting that they abandoned the updraft. These nonmeteorological echoes within the cloud required filtering. A series of filters were developed and tested and then applied to the radar data to objectively remove pixels contaminated with these bird echoes. When the filters were tested, the filtered data were viewed manually to ensure that nonmeteorological echoes were being removed from the Z_H and Z_{DR} fields. The final filtering process, described below, was our best solution to remove anomalous values of Z_H and Z_{DR} without deleting important meteorological data.

Before filtering, a matrix of values consisting of the standard deviations of the unfiltered logarithmic Z_{DR} values within each slice s at each time t for the lifetime of the cloud, $\sigma_{ZDR\text{-}u}(s, t)$, was calculated.

The first filter was applied to remove Z_{DR}, Z_H pairs where $Z_{DR} \geq 1$ dB and $Z_H < 0$ dBZ. The second filter eliminated Z_H, Z_{DR} pairs where the Z_{DR} value was less than -1 dB or greater than 3 dB. Values filtered using these criteria should not occur in drizzle. A third filter was applied to data that survived the first two filters. Birds often produced V_R values substantially different from those in the cloud and rain shaft. Because of the small size of trade wind clouds, pixels in uncontaminated clouds normally had nearly identical V_R within a single slice. To remove bird echo, pixels that had a V_R value at least 3.5 m s^{-1} different than the median velocity within a single slice were removed. The 3.5 m s^{-1} value, chosen after considerable testing, was found to be the best value to retain the cloud signal while removing clearly anomalous data.

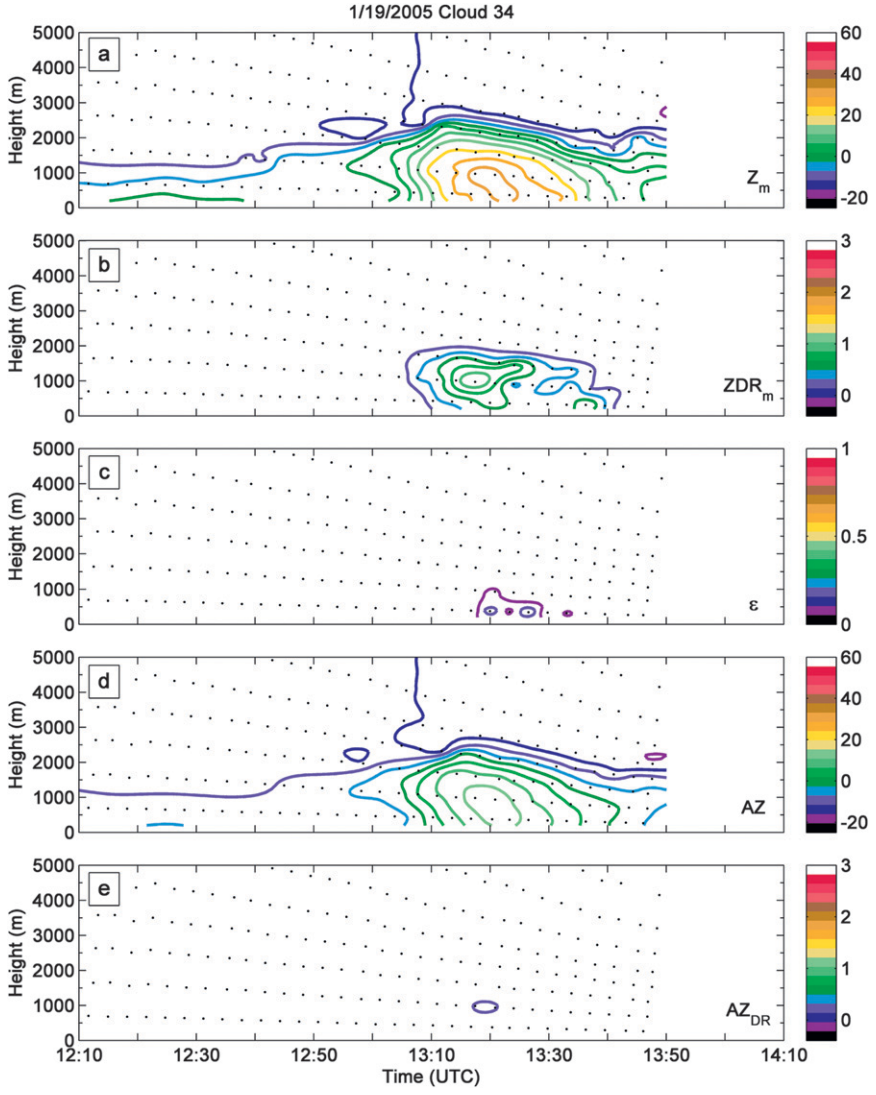

FIG. 7. As in Fig. 4, but for cloud 34 on 19 Jan 2005.

A fourth and final filter was applied based on the standard deviation of the logarithmic Z_{DR} field. First, a matrix of values consisting of the standard deviations of the *filtered* logarithmic Z_{DR} values within each slice s at each time t for the lifetime of the cloud, $\sigma_{ZDR\text{-}f}(s, t)$, was calculated. The maximum value of $\sigma_{ZDR\text{-}f}(s, t)$ within the matrix, $\sigma_{ZDR\text{-}f}(\max)$, was determined. The filter was applied only to slices where $\sigma_{ZDR\text{-}u}(s, t) > \sigma_{ZDR\text{-}f}(\max)$. When this condition was true, pixels with $Z_{DR} = 3 \times \sigma_{ZDR\text{-}f}(s, t)$ were removed.

Once all the slices composing a cloud were filtered, the maximum reflectivity factor Z_m and maximum differential reflectivity ZDR_m on each slice were recorded. For slices where $Z_m > 7$ dBZ, the spatial correlation coefficient (ε) between the logarithmic values of Z_H and Z_{DR} across the cloud on each slice was calculated using Pearson's correlation coefficient:

$$\varepsilon = \frac{n\sum_n (Z_m)_n (\mathrm{ZDR}_m)_n - \sum_n (Z_m)_n \sum_n (\mathrm{ZDR}_m)_n}{\left\{\sqrt{n\left[\sum_n (Z_m)_n^2\right] - \left[\sum_n (Z_m)_n\right]^2}\right\}\left\{\sqrt{n\left[\sum_n (ZDR_m)_n^2\right] - \left[\sum_n (ZDR_m)_n\right]^2}\right\}}, \quad (1)$$

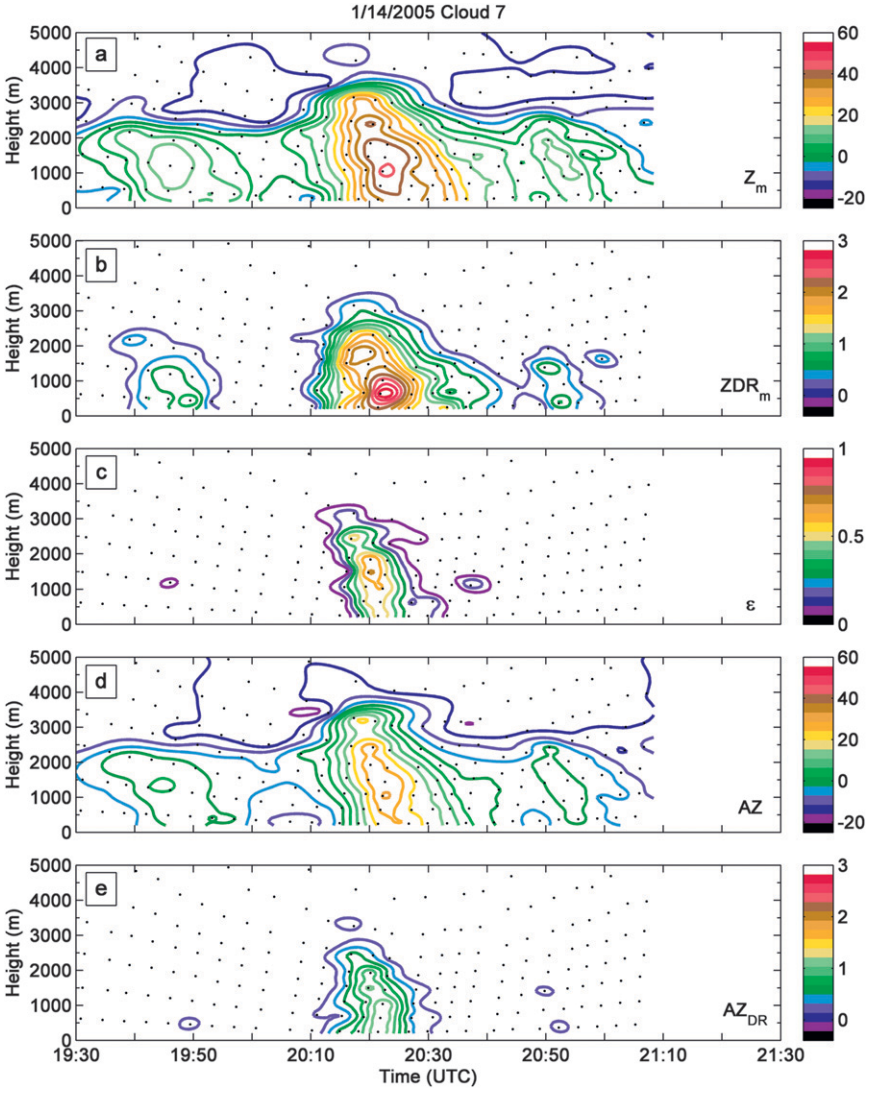

FIG. 8. As in Fig. 4, but for cloud 7 on 14 Jan 2005.

where n is the number of data points on the slice. The variable ε provides a quantitative estimate of the degree to which large raindrops coincide with regions of high Z_H. A Z_m threshold was chosen to avoid Bragg scattering that results from small-scale variations in the refractive index (Knight and Miller 1993). In clouds dominated by Bragg scattering, there should be no correlation between Z_H and Z_{DR}. Snodgrass et al. (2009) examined the transition between Bragg and Rayleigh scattering using collocated satellite and radar data from RICO (Fig. 2). They showed a distinct break around 5 dBZ, confirming earlier findings of Knight and Miller (1998). In this work, we chose a more conservative value, 7 dBZ, to ensure that the returned echo was dominated by Rayleigh scattering from raindrops. We note that Knight et al. (2008) stated that poor correlation was common between the Z_H and Z_{DR} fields in clouds observed during RICO. In this work we show that ε exceeded 0.5 in 61% of the clouds studied, and it exceeded 0.7 in 15%.

Knight et al. (2008) calculated the "average" values of Z_H and Z_{DR} (AZ and AZ_{DR}) that would result if single radar pulse volume were fitted in space to a whole slice. For comparison with Knight et al. (2008) and as an additional diagnostic we have also adopted this approach. Equations for estimating the areal average values on a slice (AZ and AZ_{DR}), presented in Knight et al. (2008), are

$$\mathrm{AZ} = 10\log\left(\sum_{\mathrm{Area}} w_a Z_H \Big/ \sum_{\mathrm{Area}} w_a\right), \qquad (2)$$

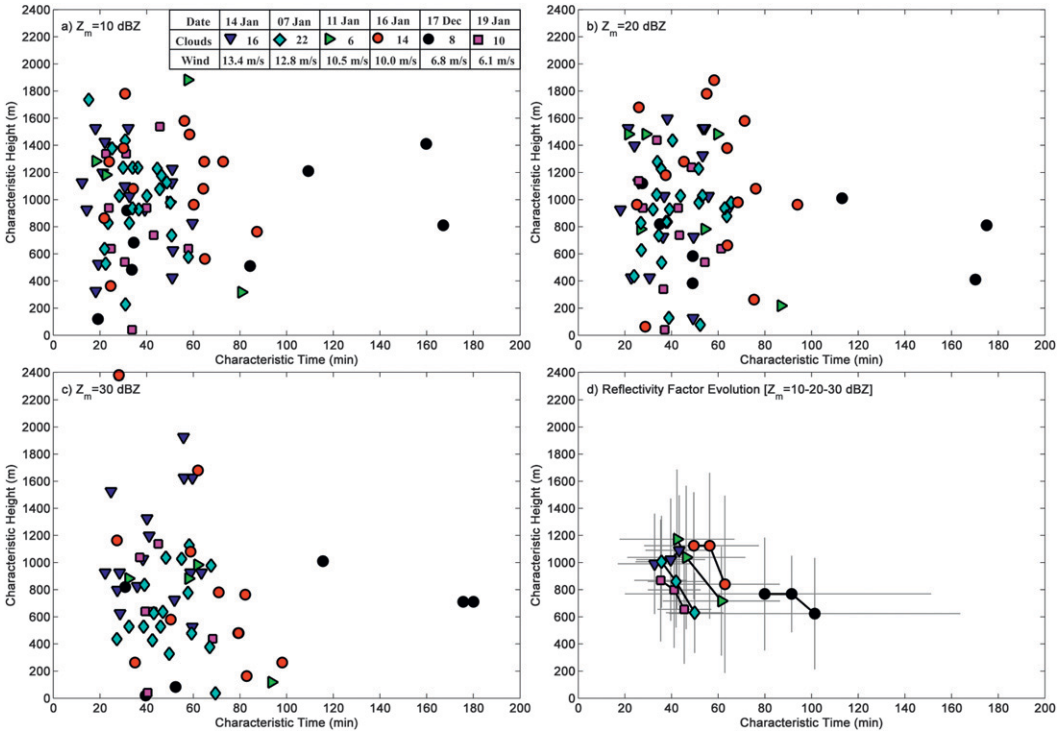

FIG. 9. The CT and CH of clouds that reached the Z_m = (a) 10-, (b) 20-, and (c) 30-dBZ threshold. (d) The evolution of the mean value of the Z_m = 10–30-dBZ thresholds for each of the six cloud populations. Vertical and horizontal bars denote the standard deviations in both time and height. On the abscissa of this and subsequent similar figures, 0 denotes cloud base, not the ocean surface.

$$\mathrm{AZ_{DR}} = 10\,\log\left(\sum_{\mathrm{Area}} w_a Z_H \Big/ \sum_{\mathrm{Area}} w_a Z_V\right), \qquad (3)$$

where Z_V refers to the equivalent radar reflectivity factor for vertical polarization. As in Knight et al. (2008), the weighting factor w_a in these equations was set to unity. Since Z_H and Z_{DR} are recorded as logarithms, obtaining the average values required recalculating the recorded data back to linear Z, both horizontal and vertical, and then converting back to logarithmic values after averaging (Knight et al. 2008).

The characteristic time (CT) for precipitation development (Göke et al. 2007) is defined here as the length of time between "cloud initiation" and the first occurrence of a chosen radar variable threshold (Fig. 3). Cloud initiation is a difficult quantity to define using S-band radar alone because of the sensitivity of the radar to both Bragg and Rayleigh scattering, since coherent echoes can be observed from precipitation, cloud, and clear air. Figure 2, adapted from Snodgrass et al. (2009), provides a reference as to when a growing cloud will be detected. This figure shows the distribution of Z_H for both clear and cloudy sky as determined by collocated data from MISR and the S-Pol radar during RICO. This figure indicates that when tracking a cloud backward in time, the cloud will typically become indistinguishable from the clear sky background when Z_H falls below approximately −5 dBZ. At close ranges the sensitivity of the radar for cloud detection could extend to as low as −20 dBZ (Knight et al. 2008), allowing some clouds to be tracked even further back in their lifetime. For this study, cloud initiation was defined as the time of the 0.5° sweep file one volume scan before the cloud was first detected by the S-band radar based on a visual analysis of Z_H for each cloud (t_0 in Fig. 3). In doing so, we assume that even though the cloud would not yet be detected by the radar for 3–4 min, it was still present and initially forming.

The end of the CT interval was defined by the first appearance of a chosen threshold value in one of the following variables: Z_m, ZDR_m, $\mathrm{AZ_{DR}}$, or ε. Three Z_m thresholds (10, 20, and 30 dBZ) were chosen to represent different stages of precipitation development within the cloud, whereas the ZDR_m and $\mathrm{AZ_{DR}}$ thresholds (ZDR_m = 1, 2 dB and $\mathrm{AZ_{DR}}$ = 1 dB) were chosen to study the first appearance of large drops during precipitation development. The ε thresholds (0.5, 0.7) were chosen to determine when the Z_H and Z_{DR} fields were becoming spatially coincident, indicating that the large

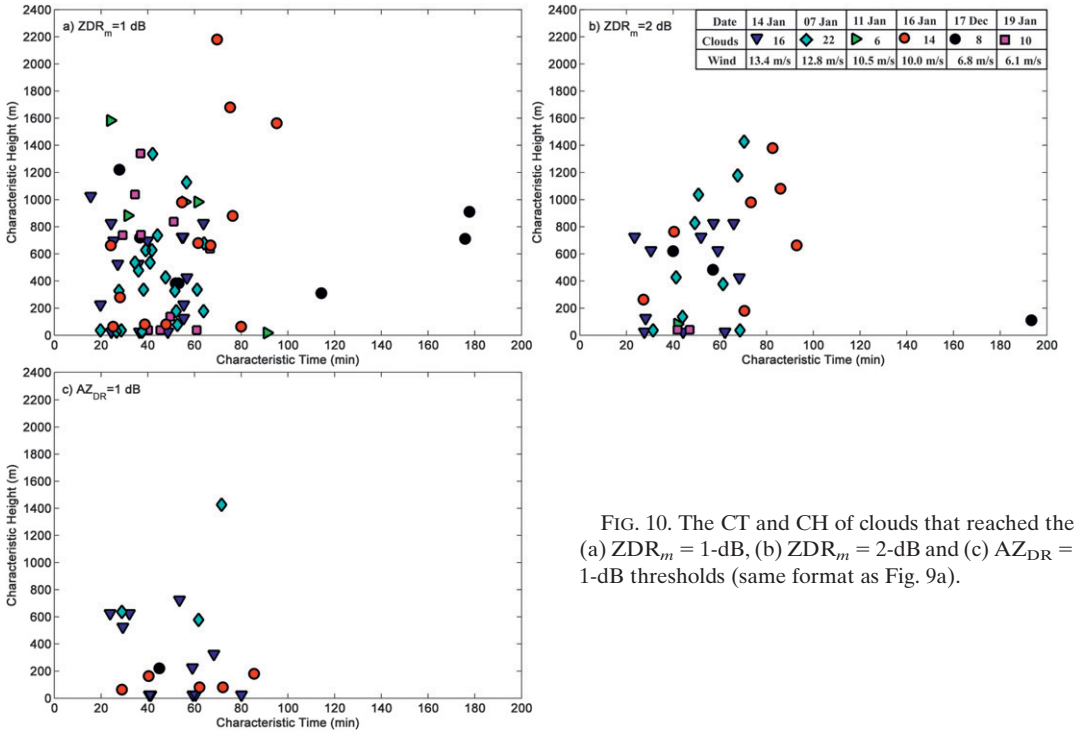

FIG. 10. The CT and CH of clouds that reached the (a) ZDR_m = 1-dB, (b) ZDR_m = 2-dB and (c) AZ_{DR} = 1-dB thresholds (same format as Fig. 9a).

drops were coincident with the heavier precipitation. The height above cloud base at which the final radar variable threshold was reached was defined as the characteristic height (CH) for precipitation formation. A CT and CH were determined for each threshold in each of the clouds analyzed. These data were then analyzed to determine if any statistically significant trends could be related to aerosol or other characteristics of the clouds.

3. Results

a. Time–height evolution

The radar evolution of each cloud was visualized using a time–height section approach (Battan 1953). Figures 4–8 display examples of the temporal and spatial evolution of Z_m, ZDR_m, ε, AZ, and AZ_{DR} that illustrate some key features of cloud evolution appearing in the broader dataset.

Figure 4 displays the radar evolution of a cloud that developed precipitation very slowly; specifically, the 10-dBZ Z_m threshold was reached 65 min after cloud initiation. During the 65-min period, the cloud was detected only at low elevations (<1200 m). After 65 min, development occurred rapidly, as the cloud reached a maximum lifetime Z_m of about 40 dBZ 15 min after the 10-dBZ Z_m threshold was surpassed. The time section also shows that large drops only started to develop after the 10-dBZ Z_m threshold was surpassed; ZDR_m values of 2 dB and AZ_{DR} values of 1 dB were concurrent with the later stages of precipitation development and appeared around the same time as the 30-dBZ Z_m threshold was surpassed. The 1-dB ZDR_m threshold was reached approximately 3 min before the 30-dBZ Z_m threshold and the 1-dB AZ_{DR} and 2-dB ZDR_m thresholds occurred approximately 6 min after the 30-dBZ Z_m threshold was reached and 3–4 min before the maximum lifetime Z_m value of 40 dBZ occurred. The 1-dB AZ_{DR} threshold was surpassed at an elevation close to cloud base about 3–4 min before the maximum lifetime Z_m value of 40 dBZ occurred. The Z_H and Z_{DR} fields were well correlated after the 10-dBZ Z_m threshold was reached, with values of ε reaching 0.63, indicating that the largest drops were coincident with the heaviest rain. The time from the first appearance of the 10-dBZ Z_m threshold to the last appearance was 45 min.

Figure 5 displays the evolution of a cloud that developed much differently than the cloud in Fig. 4. In this cloud, the 10-dBZ Z_m threshold was reached within 22 min of cloud initiation, and the maximum lifetime Z_m of 45 dBZ was reached within 30 min of cloud initiation. The vertical development of the precipitation echo occurred rapidly after cloud initiation, reaching an altitude of ~4000 m. The first appearance of large drops once again lagged the first appearance of rain. The 1-dB ZDR_m threshold was reached approximately 4 min after the 10-dBZ Z_m threshold and the 2-dB ZDR_m and 1-dB AZ_{DR} thresholds

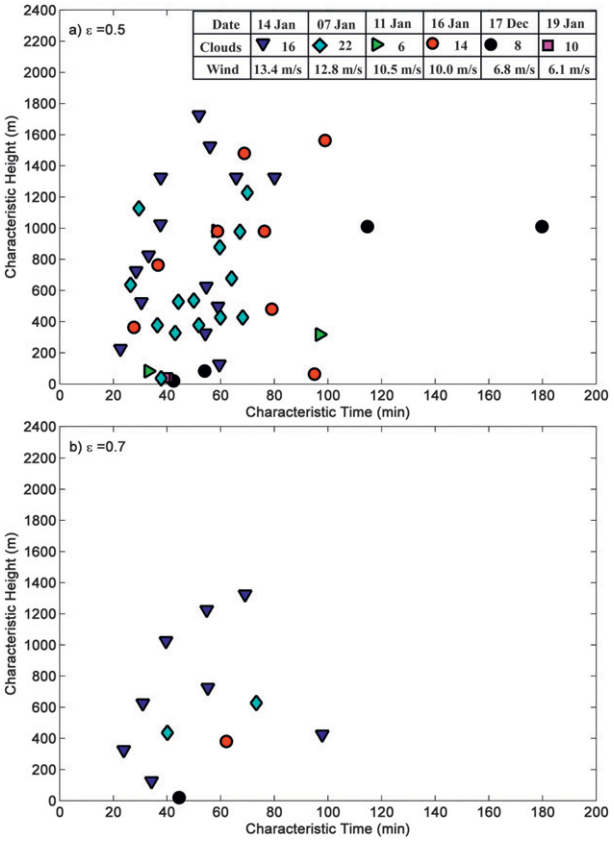

FIG. 11. The CT and CH of clouds that reached the (a) $\varepsilon = 0.5$ and (b) $\varepsilon = 0.7$ thresholds (same format as Fig. 9a).

occurred at the same time as the 30-dBZ Z_m threshold. The 30-dBZ Z_m threshold was reached only 7 min after the 10-dBZ Z_m threshold was surpassed. The 2-dB ZDR$_m$ and 1-dB AZ$_{DR}$ plots indicate that large drops were present throughout the depth of the cloud around 25 min after cloud initiation, with the largest drops closer to cloud base than cloud top. Again, once the 10-dBZ Z_m threshold was surpassed, the Z_H and Z_{DR} fields became progressively well correlated, with ε reaching a maximum value of 0.59. The time from the first appearance of the 10-dBZ Z_m threshold to the last appearance was 65 min.

The clouds in Figs. 4 and 5 had lifetimes of almost 120 min. Some clouds, such as the cloud in Fig. 6, had much shorter lifetimes. Variation was also seen in the vertical development of the precipitation echoes. Figures 6 and 7 show examples of clouds that had similar maximum lifetime Z_m values of ~30 dBZ, but the altitudes at which this maximum was observed—2200 and 1100 m, respectively—differed by ~1 km. The ZDR$_m$ fields evolved differently as well; the cloud in Fig. 6 reached ZDR$_m$ values of 2 dB whereas the cloud in Fig. 7 never exceeded 1 dB. In Fig. 6 the Z_m = 10-dBZ threshold led the occurrence of the 1-dB ZDR$_m$ threshold by 6 min and the two fields were only weakly correlated with a maximum ε value of 0.52. In Fig. 7 the Z_H and Z_{DR} fields were poorly correlated with the maximum ε reaching only 0.25. The time from the first appearance of the 10-dBZ Z_m threshold to the last appearance in Figs. 6 and 7 was 25 and 35 min, respectively.

An interesting feature of some RICO clouds was a pulsation in precipitation. Figure 8 shows an example of a cloud that developed rain shafts three times within the cloud's 100-min lifetime. Out of 76 clouds, 39 pulsated twice within their lifetime and 8 pulsated 3 times. Feingold et al. (2010) noted similar oscillations in convection associated with marine stratocumulus, although it is not clear that the mechanism proposed for those clouds applies to the trade wind cumulus observed here. The mean time between pulses, defined by successive maxima in Z_m, was approximately 19 min.

TABLE 4. Results of the nonparametric multi-response permutation procedure. The values in this chart are the calculated probability (p values) that the data partitions are not disjoint.

15 pairs (dates)	10-dBZ Z_m	20-dBZ Z_m	30-dBZ Z_m	1-dB ZDR$_m$	2-dB ZDR$_m$	1-dB AZ$_{DR}$	0.5ε	0.7ε
14 and 7 Jan	0.97	0.23	0.0007	0.67	0.499	0.152	0.167	0.54
14 and 11 Jan	0.61	1.00	0.20	0.0519			0.43	
14 and 16 Jan	0.16	0.32	0.026	0.11	0.15	0.42	0.66	
14 Jan and 17 Dec	0.0066	0.0074	0.00019	0.0026	0.57		0.048	
14 and 19 Jan	0.77	0.37	0.085	0.73	0.08		0.014	
7 and 11 Jan	0.46	0.34	0.50	0.0153			0.87	
7 and 16 Jan	0.11	0.014	0.059	0.053	0.608	0.018	0.21	
7 Jan and 17 Dec	0.001	0.0024	0.0017	0.0007	0.48		0.027	
7 and 19 Jan	0.55	0.85	0.92	0.35	0.11		0.0098	
11 and 16 Jan	0.77	0.78	0.63	0.477			0.65	
11 and 17 Jan	0.057	0.13	0.19	0.186			0.46	
11 and 19 Jan	0.30	0.46	0.60	0.305				
16 Jan and 17 Dec	0.023	0.039	0.078	0.13	0.44		0.23	
16 and 19 Jan	0.14	0.086	0.26	0.419	0.028		0.018	
17 Dec and 19 Jan	0.082	0.05	0.057	0.048			0.15	

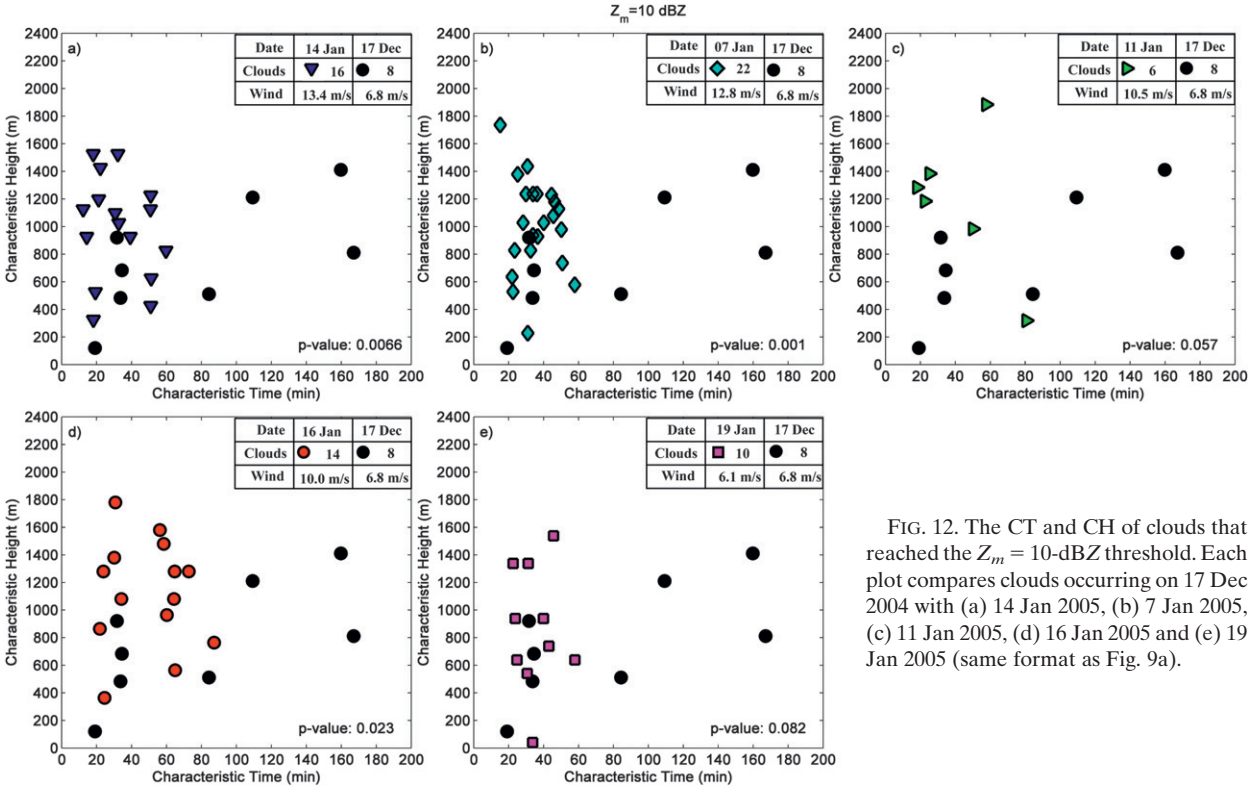

FIG. 12. The CT and CH of clouds that reached the Z_m = 10-dBZ threshold. Each plot compares clouds occurring on 17 Dec 2004 with (a) 14 Jan 2005, (b) 7 Jan 2005, (c) 11 Jan 2005, (d) 16 Jan 2005 and (e) 19 Jan 2005 (same format as Fig. 9a).

The average time between the first occurrence of the 10-dBZ Z_m threshold and the last occurrence for all clouds where the cloud dissipation stage was observed was 35 min, with a standard deviation of 17 min and extreme values of 81 and 6 min. For clouds where the 10-dBZ Z_m threshold occurred multiple times within the cloud, each pulsation was counted as a separate cloud to generate these statistics.

b. *Characteristic time versus height for the cloud populations*

The scatterplots of CT versus CH shown in Figs. 9–11 were used to compare the radar evolution of the clouds on the six days with different GCN concentrations (Fig. 1; Table 2). Each point in these diagrams represents the time and height at which an individual cloud reached a specified threshold. Figures 9a–c display the time and height at which the cloud populations reached Z_m = 10, 20, and 30 dBZ, respectively. Figure 9a, which nominally represents the first occurrence of rain within the cloud, shows that clouds can develop precipitation in as little as 12 min. Figure 9c shows that heavier rainfall can develop within 22 min. The plots also reveal that precipitation initiation in shallow marine cumuli has a wide time range, as the CT for precipitation initiation (Fig. 9a) in some clouds was as large as 170 min. Considering the cloud population on 14 January 2005 alone (Fig. 9a, blue triangles), we see that CT and CH, even on a single day, are far from uniform. Assuming that the GCN were homogeneously distributed, the spread in CT and CH on a single day implies that something more than GCN concentrations is affecting precipitation development. The scatter in CH also indicates that precipitation formation via the collision/coalescence process can lead to the first appearance of rain at very different elevations within the cloud.

A large portion of the cloud sample (62 out of 76 analyzed clouds) reached the Z_m = 30-dBZ threshold. Once the Z_m = 10-dBZ threshold was reached, the Z_m thresholds of 20 and 30 dBZ followed quickly. We interpret this to mean that once the collision/coalescence process began, precipitation intensified rapidly.

Visualizing the differences in cloud evolution on different days was aided by calculating the mean CT and CH at which clouds on a specific day reach a given threshold (Fig. 9d). One observation that becomes clear is the separation of 17 December 2004 from the rest of the cloud populations. Furthermore, the CH of Z_m decreases with the exception of 14 January 2005, where each Z_m threshold has a higher CH than the last. Another interesting observation is that CT decreases with increasing low-level wind speed for each Z_m threshold with one exception—19 January 2005. This day, which

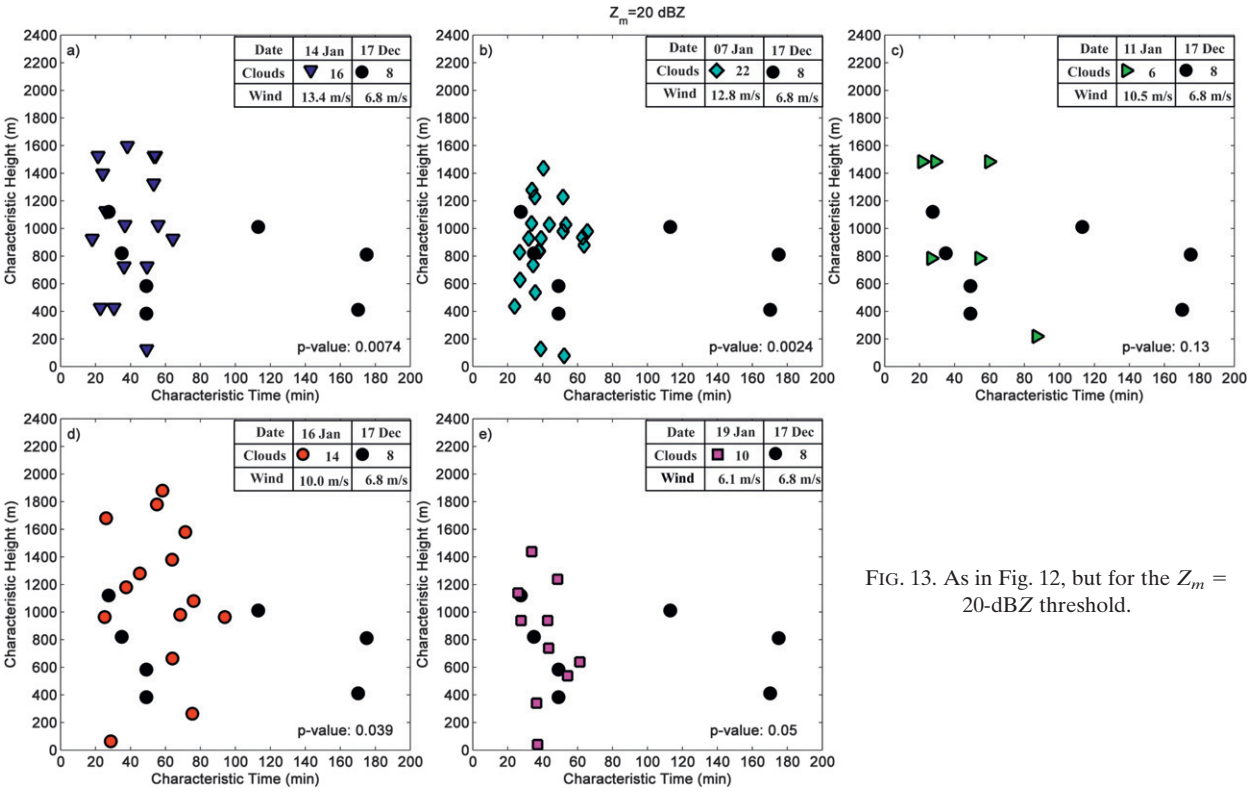

FIG. 13. As in Fig. 12, but for the Z_m = 20-dBZ threshold.

had the weakest low-level wind speeds, had CTs similar to 14 January 2005 (the strongest wind speed day).

The CT and CH for the 1-dB ZDR_m, 2-dB ZDR_m, and 1-dB AZ_{DR} thresholds, an indication of the time and location that the larger drops were present in the clouds, are shown in Figs. 10a–c. The number of clouds that reached thresholds of 2-dB ZDR_m and 1-dB AZ_{DR} (33 and 20 clouds, respectively; Figs. 10b,c) was significantly diminished compared to the number of clouds that reach the 1-dB ZDR_m threshold (74 out of 76; Fig. 10a). The 2-dB ZDR_m threshold, indicative of very large drops, was generally reached earlier in time and higher in the clouds on days with stronger low-level wind speeds. Although at least one cloud from each of the six days reached the 2-dB ZDR_m threshold, the threshold was generally reached closer to cloud base on days with weaker low-level wind speeds. The number of clouds that reach the 1-dB AZ_{DR} threshold, an indication of the average drop size within the cloud, was even smaller than those that reached the 2-dB ZDR_m threshold (Fig. 10c). Clouds on days with higher wind speeds reached the 1-dB AZ_{DR} threshold at a higher CH compared to the remaining clouds.

Sixty-one percent (46 out of 76 clouds) of the clouds reached the 0.5 ε threshold (Fig. 11a), and 15 percent (12 out of 76 clouds) reached the 0.7 ε threshold (Fig. 11b). The degree of correlation between the Z_H and Z_{DR} fields appeared to be related to low-level wind speed. Eighty-three percent of the clouds that reached the 0.7 ε threshold occurred on the two days with the strongest low-level wind speeds.

c. *Test of the giant nuclei hypothesis*

The nonparametric multi-response permutation procedure developed by Mielke et al. (1981) was used to determine the statistical significance in the precipitation evolution that can be related to the initial GCN concentration. This procedure uses a resampling technique to determine the level of significance of data clustering in datasets for which the underlying distribution is unknown (e.g., the data are not normally distributed). For each pair of cloud populations we tested the null hypothesis that the observed clustering of the data was a chance random event; that is, that the average distance between members of each observed population was not significantly different from all the other possible groupings of the same data (Göke et al. 2007). Table 4 summarizes the results of the statistical test. Column 1 of Table 4 indicates the pair of days tested and columns 2–9 report the probability value (p value) that the two populations of clouds on the different days have significantly different characteristic behavior (i.e., they separate into disjoint populations). If a day had fewer than two clouds that met a specific threshold

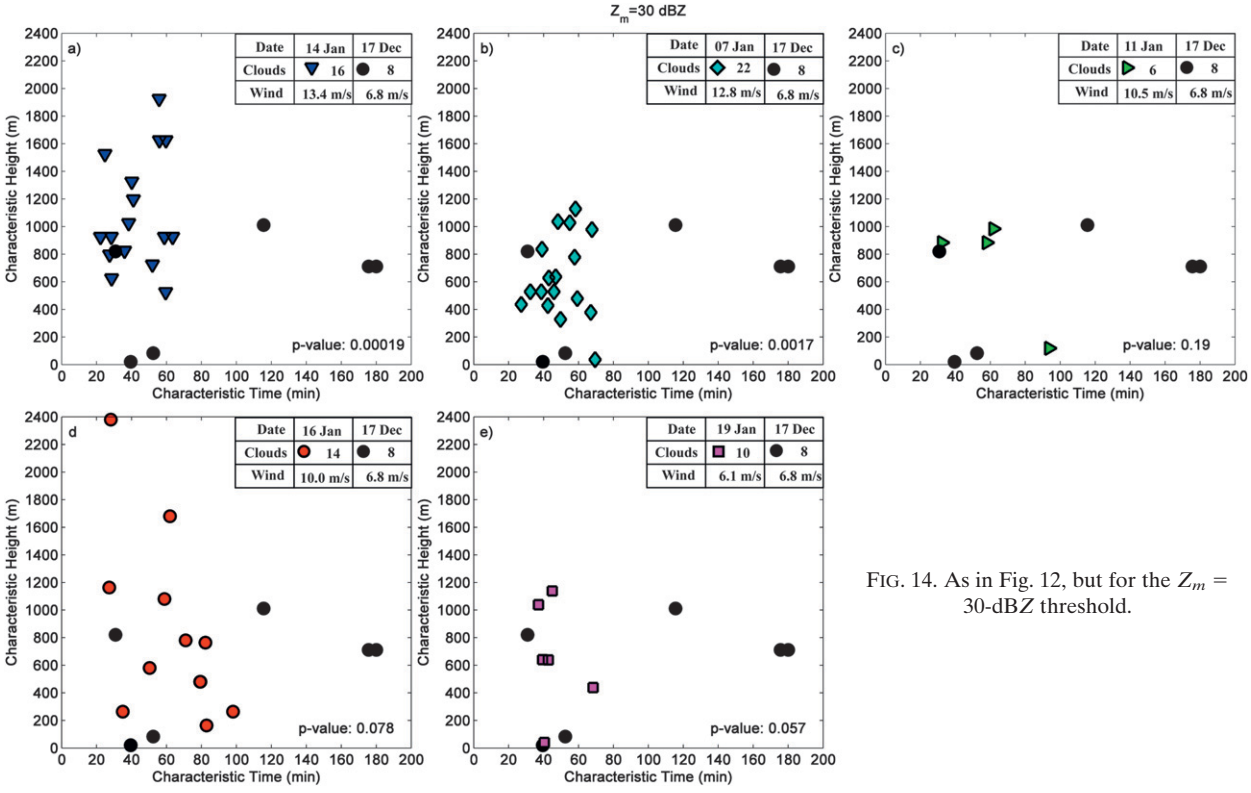

FIG. 14. As in Fig. 12, but for the Z_m = 30-dBZ threshold.

the statistics could not be calculated and those areas of Table 4 were left blank.

In total, 87 statistical calculations were made, one for each pair of cloud populations at each threshold where enough data were available. The statistical results reveal that 73.5% of the cloud populations were not statistically disjoint at the 95% confidence level. Twenty-three pairs were disjoint at the 95% confidence level and 33 pairs were disjoint at a confidence level of 90%.

A few trends appear in Table 4. First, the population of clouds on 17 December 2004, which had weak low-level wind speeds, stood out as being visually distinct from all other cloud populations (Fig. 9d). The statistical results in Table 4 confirm that this population of clouds is significantly different from the other cloud populations at each of the chosen thresholds, with a few exceptions. Figures 12–17 depict CT versus CH for each cloud population compared to 17 December 2004. At the 10-dBZ Z_m threshold, the cloud population on 17 December 2004 is statistically disjoint from the other cloud populations because of differences in CT; in general all the other cloud populations reached the specified thresholds more quickly than 17 December 2004. Figures 13–16 depict plots similar to those of Fig. 12 but for the 20- and 30-dBZ Z_m, 1-dB ZDR_m, and 0.5 ε thresholds, respectively. These figures also show that cloud populations that are statistically distinct from 17 December 2004 reached the specified thresholds more quickly. Furthermore, the cloud populations that are not statistically distinct (Figs. 13c, 14c, 15c,d, 16c,d,e) had relatively similar CT and CH. Notice that two cloud populations (14 January 2005 and 7 January 2005) that had strong low-level wind speeds were significantly distinct from 17 December 2004 at all of the specified thresholds.

The second trend observed in the statistics was that the population of clouds on 14 January 2005 was statistically disjoint from four of the other five cloud populations at the 30-dBZ Z_m threshold (Fig. 17). The p values, with the exception of Fig. 17b, were very small ($p < 0.085$), indicating the likelihood that each partition is disjoint is very high. The statistical results confirm the visual observations in Fig. 9d—the mean CT and CH at which the population of clouds on 14 January 2005 reach the 30-dBZ Z_m threshold appears visually distinct from all of the other cloud populations. On average, the population of clouds on 14 January 2005 reached the 30-dBZ Z_m threshold at a higher CH than the other cloud populations.

It is noteworthy that Table 4 is not completely filled in. Most of the population pairs that could not be statistically tested occurred because the thresholds of 2-dB ZDR_m, 1-dB AZ_{DR}, and 0.7 ε were never reached. For the most part, only cloud populations that had the strongest

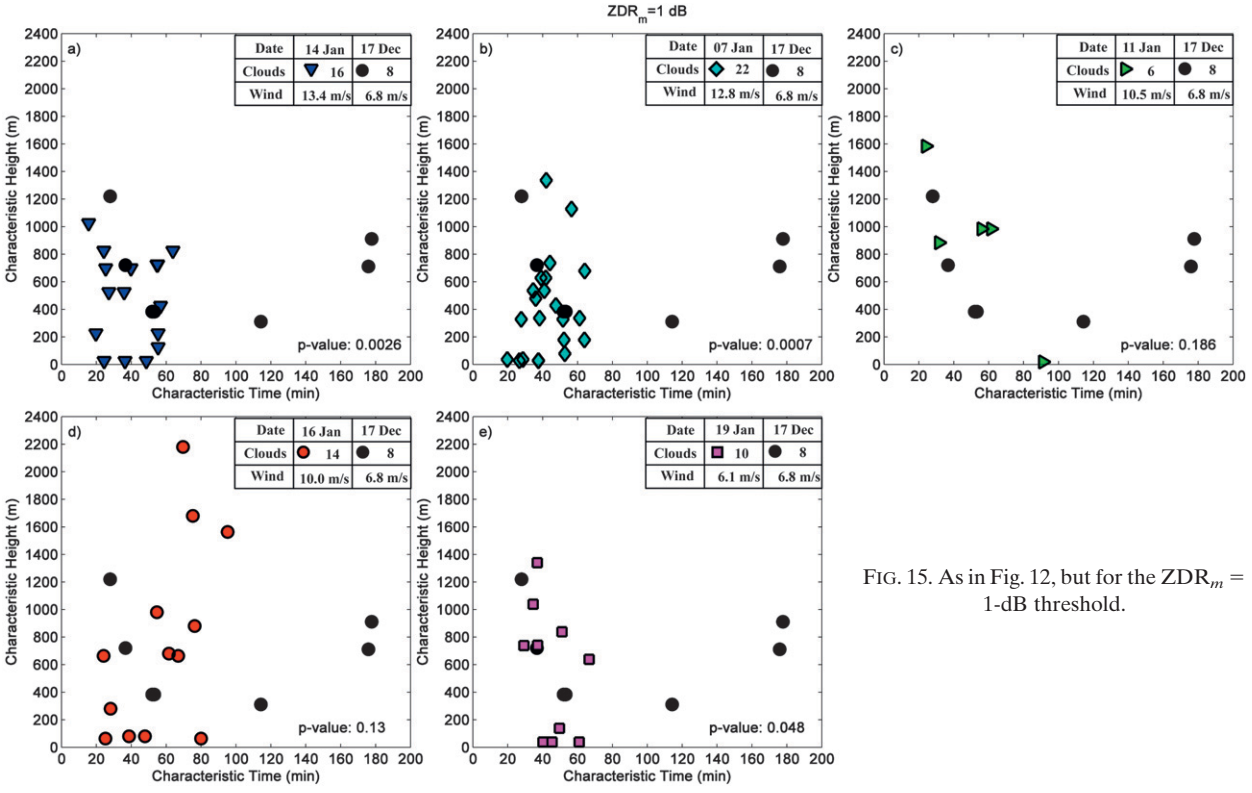

FIG. 15. As in Fig. 12, but for the ZDR$_m$ = 1-dB threshold.

low-level winds reach thresholds of 2-dB ZDR$_m$, 1-dB AZ$_{DR}$, and 0.7 ε.

4. Discussion

At first glance, our data analysis seems to indicate that GCN are important for precipitation development. The CT versus CH scatterplots for the Z_m thresholds (Fig. 9d) show that, on average, precipitation development occurs more quickly in the population of clouds on 14 January 2005 (fastest low-level wind speeds, largest concentration of GCN) than in any other population of clouds. Precipitation initiation took the longest on 17 December 2004 (weak low-level wind speeds, small concentration of GCN). Interestingly, the other cloud populations also reach the specified Z_m thresholds in order of fastest to slowest low-level wind speed with one very important exception: the population of clouds on 19 January 2005 (slowest low-level wind speeds, smallest GCN concentration) reached the specified Z_m thresholds at times comparable to the population of clouds on 14 January 2005. The statistical results (Table 4; Fig. 18) show that the population of clouds on 14 and 19 January 2005 are not statistically disjoint at the 10- and 20-dBZ Z_m thresholds, despite having the largest difference in low-level wind speed and the largest difference in GCN concentrations. These two cloud populations reached the specified thresholds around the same CT and CH and could not be distinguished on the basis of GCN concentrations. If GCN were important for precipitation initiation, we would expect to see a shorter time for precipitation development with increased GCN concentrations. These results indicate that the rate of precipitation formation is not related to GCN concentrations.

Other observations also indicate the lack of importance of GCN in precipitation development. First, the extremely large spread in CT on 17 December 2004, which ranges from 20 min to almost 170 min at the 10-dBZ Z_m threshold, cannot be explained by the GCN concentration alone and implies that other processes may be more important for precipitation formation. Another observation that degrades the importance of GCN for precipitation formation is the range in elevation at which individual cloud populations reach any of the specified thresholds. The CH ranged from slightly above cloud base to as high as 2400 m above cloud base. The spread in CH that can be seen in any of the CT versus CH scatterplots indicates that collision and coalescence occur at all levels within the clouds and suggests that GCN are having little if any influence on the height at which precipitation formation occurs.

Additionally, the statistical results from the comparison of the clouds on 14 January 2005 at the 30-dBZ Z_m

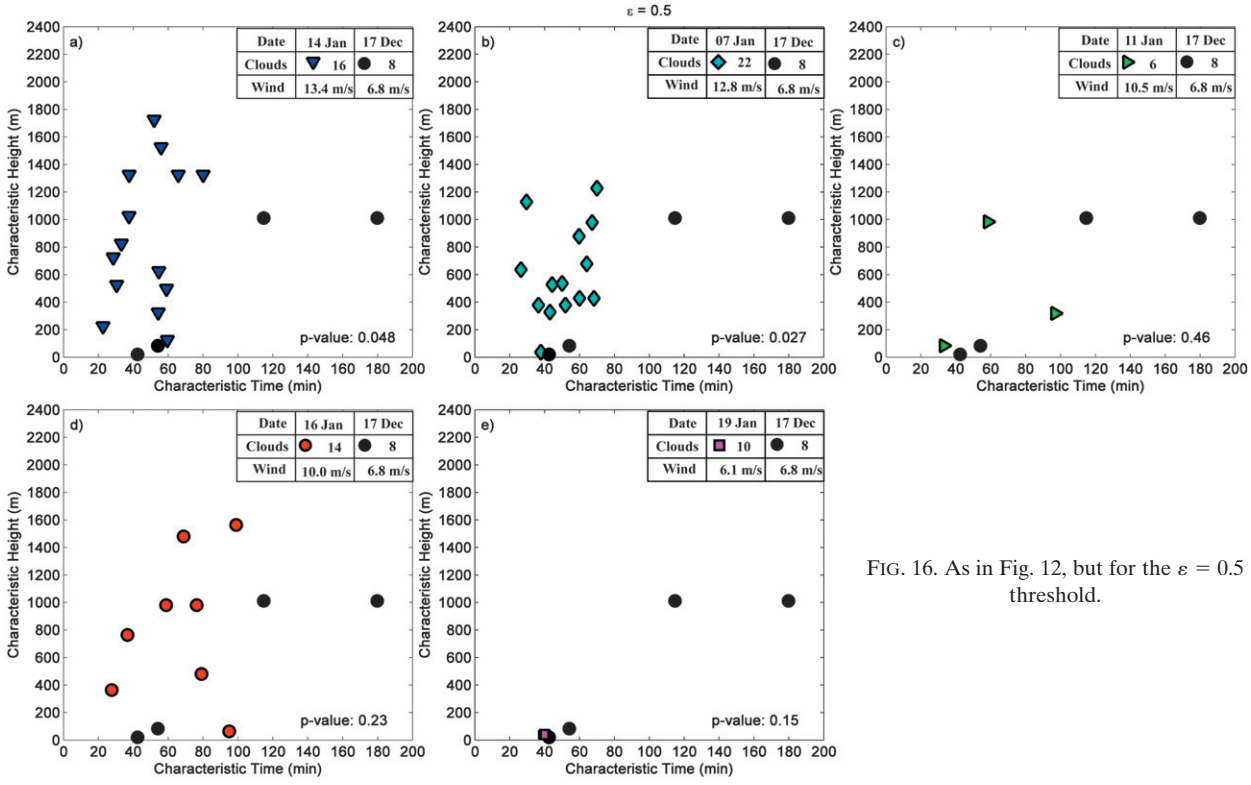

FIG. 16. As in Fig. 12, but for the $\varepsilon = 0.5$ threshold.

threshold to all other cloud populations (Fig. 17) provide more evidence against GCN as having a strong influence on rapid warm rain initiation. In general, the clouds on 14 January 2005 reach the 30-dBZ Z_m threshold at higher elevations within the cloud compared to most other cloud populations. The elevation distinction between these cloud populations indicates that updraft strength is more likely to dictate the height at which the thresholds are reached and points to the more important role of dynamical forcing in warm rain formation.

This result is consistent with the findings of Snodgrass et al. (2009) concerning rainfall and mesoscale cloud organization. Figures 19a–f display PPI images representative of the mesoscale cloud organization on each of the 6 days analyzed. Figures 19a and 19b show the mesoscale cloud organization present on 17 December 2004 and 19 January 2005, respectively; 17 December 2004 is shown at higher magnification so that the cloud organization is more evident. On 17 December 2004, the cloud field was characterized by wind-parallel cloud streets, whereas the mesoscale cloud organization on 19 January 2005 consisted of shallow cumulus clusters often arranged in arc-shaped formations characteristic of outflow boundaries. The microphysical evolution based on the radar data was statistically disjoint on these two days despite their similar low-level wind speeds.

Comparing the mesoscale cloud organizations on 14 and 19 January 2005 (Figs. 19c and 19b, respectively) reveals that both days were dominated by shallow cumulus clusters arranged in arc-shaped formations. Despite the difference in low-level wind speeds, these cloud populations had statistically similar CT and CH for the 10-, 20-, and 30-dBZ Z_m thresholds. These results imply that mesoscale cloud organization and subsequent forcing associated with each system had a strong influence on the rate at which precipitation formed.

The influence of GCN is not completely lost, however. With a few exceptions, only cloud populations on days with the strongest low-level wind speeds had ZDR_m values consistent with the presence of large drops above cloud base. Some of the clouds on weak low-level wind speed days do reach thresholds of 2-dB ZDR_m and 1-dB $\mathrm{AZ}_{\mathrm{DR}}$; however, they represent only a small fraction of the total number of clouds tracked on that day. For those clouds it was determined that these thresholds were reached after the 30-dBZ Z_m threshold—implying that the large drops took their entire growth trajectory to become this large (e.g., Szumowski et al. 1999). The Z_H and Z_{DR} fields show better correlation (i.e., large values of Z_H and Z_{DR} occur at the same time and in the same region of the cloud) when low-level wind speeds are stronger. While the cloud populations on 14 and 19 January 2005 are not

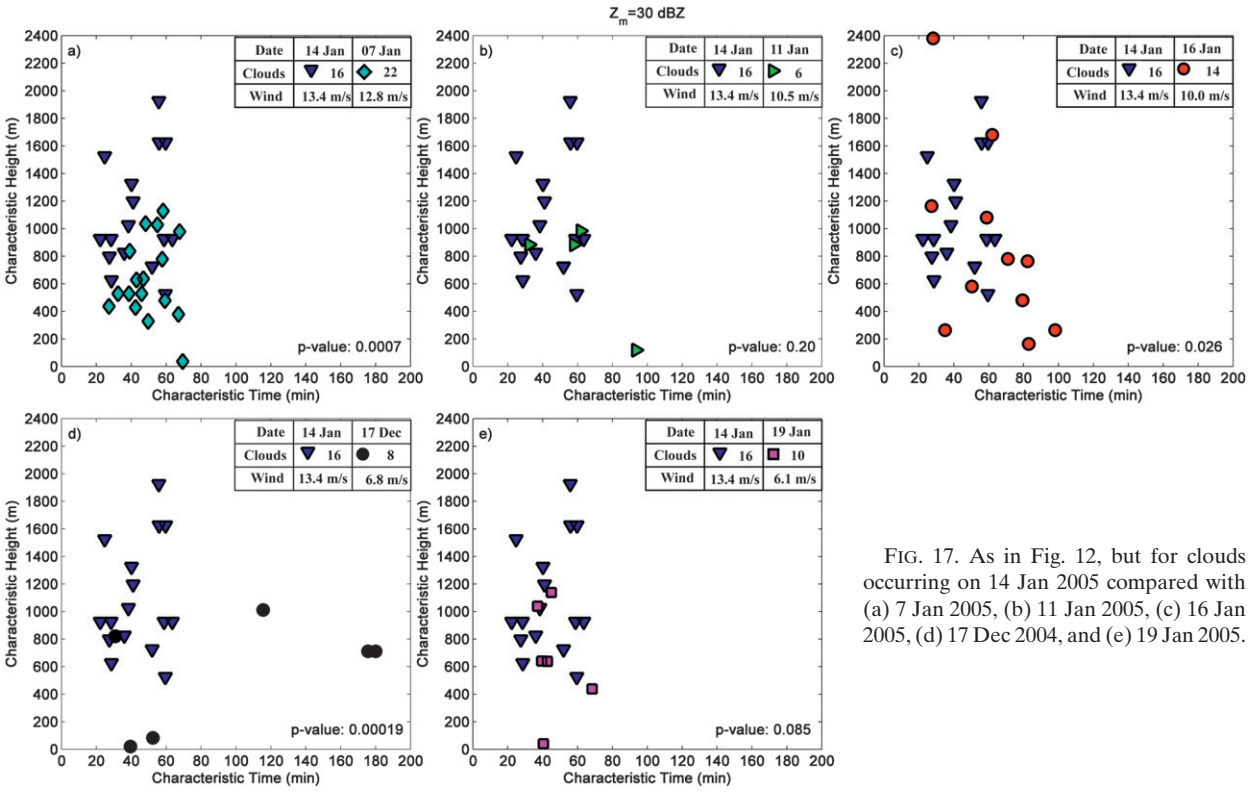

FIG. 17. As in Fig. 12, but for clouds occurring on 14 Jan 2005 compared with (a) 7 Jan 2005, (b) 11 Jan 2005, (c) 16 Jan 2005, (d) 17 Dec 2004, and (e) 19 Jan 2005.

statistically significantly different at the 10- and 20-dBZ Z_m thresholds, the populations are statistically disjoint at the 2-dB ZDR_m threshold and the 0.5 ε threshold, indicating that GCN concentrations may be leading to the presence of a few large drops at the large end tail of the rain drop size distributions.

5. Summary

This paper presented a statistical analysis of the characteristic height and time at which precipitation passes through distinct stages in its evolution as defined by the equivalent radar reflectivity factor at horizontal polarization Z_H, the differential reflectivity Z_{DR}, and the spatial correlation between, and averages of these variables. The data for this study were collected by the NCAR S-band dual-polarization (S-Pol) Doppler radar, which was located on the island of Barbuda at the north end of the Lesser Antilles, by the NSF–NCAR C130 aircraft during low-level flights over the open ocean within the radar domain, and from soundings launched near the radar, all during the RICO field campaign. The dataset consisted of 76 trade wind cumuli that were tracked from early echo development through rainout over six days of the field project. Analysis days were chosen based on the results of Colón-Robles et al. (2006), which show that GCN concentrations are a strong function of near-surface wind speed. Populations of trade wind clouds used in the statistical analyses were segregated based on the GCN measurements made during low-level aircraft flights on days when the 76 trade wind cumuli were observed.

The key findings of this paper are as follows:

1) The characteristic height and time at which radar echoes in the developing cumulus reached specified threshold Z_m values of 10, 20, and 30 dBZ could not be related to the GCN concentration in the ambient environment.
2) Rather, the rate at which precipitation developed in the clouds appeared to be related to the mesoscale updraft forcing as suggested by the cloud organization. Clouds occurring on boundary layer rolls were observed to remain coherent for 170 min before reaching a 10-dBZ Z_m threshold while clouds associated with arc-shaped outflows having similar GCN concentrations reached the 10-dBZ Z_m threshold in as little as 20 min. These data support the argument that GCN do not influence the rate of precipitation development in trade wind cumuli.
3) The threshold values of 1- and 2-dB ZDR_m, 1-dB AZ_{DR}, and 0.5 and 0.7 ε were reached, with very few

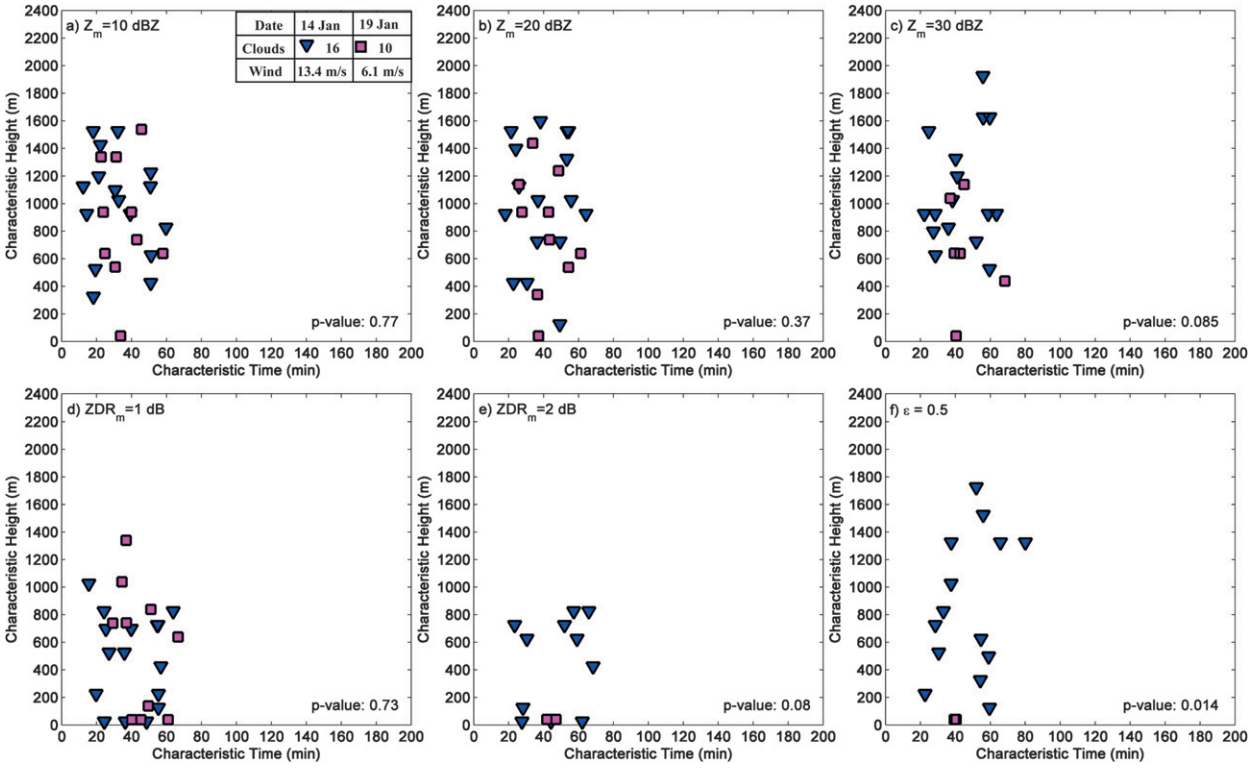

FIG. 18. Comparison of the CT and CH of clouds on 14 and 19 Jan 2005 at Z_m = (a) 10, (b) 20, and (c) 30 dBZ; at ZDR_m = (d) 1 and (e) 2 dB; and (f) at $\varepsilon = 0.5$.

exceptions, only by clouds occurring on days with high GCN concentrations. On the days that were exceptions, these threshold values were almost always achieved near cloud base. On the high GCN days they were achieved at higher altitudes within the clouds. These data suggest that although GCN had no influence on the rate of precipitation development, they did contribute to a modification of the rain drop size distribution within the clouds.

This paper is the sixth in a series from the RICO experiment—the others are Colón-Robles et al. (2006), Hudson and Mishra (2007), Knight et al. (2008), Reiche and Lasher-Trapp (2010), and Arthur et al. (2010)—to investigate the role of GCN in precipitation development in trade wind cumuli. Each paper took a different approach to the analysis of the RICO dataset and independently arrived at a similar conclusion based on interpretation of the results. From these six studies, and from past results from other locations (e.g., Woodcock et al. 1971, Szumowski et al. 1999), we may therefore conclude with reasonable certainty that GCN, which over the ocean are undoubtedly composed of sea salt, have no significant influence on the rate at which the *bulk* of the precipitation forms in trade wind clouds. Szumowski et al. (1999), studying trade wind clouds near Hawaii, demonstrated that individual raindrops can form on GCN and grow to large raindrops within 15–20 min. In the trade wind clouds observed in RICO, such large drops, if they exist, may influence the shape of the drop size distribution, but not in a way that matters to the rate of precipitation formation. The findings of Colón-Robles et al. (2006), Snodgrass et al. (2009), Reiche and Lasher-Trapp (2010), and Arthur et al. (2010) together with this paper imply that cloud height (i.e., the updraft strength) appears to be the most important factor leading to rain. Evidence presented in Snodgrass et al. (2009) and in this paper that mesoscale cloud organization is closely tied to precipitation evolution makes a strong case that dynamical forcing is the key parameter driving precipitation in trade wind clouds.

Acknowledgments. This research was funded by the National Science Foundation (NSF) under Grants ATM-03-46172 and ATM-08-54954. We thank the staff of NCAR EOL for their incredible contributions to make RICO a success, and Matt Freer for his help in developing computer programs used in this research.

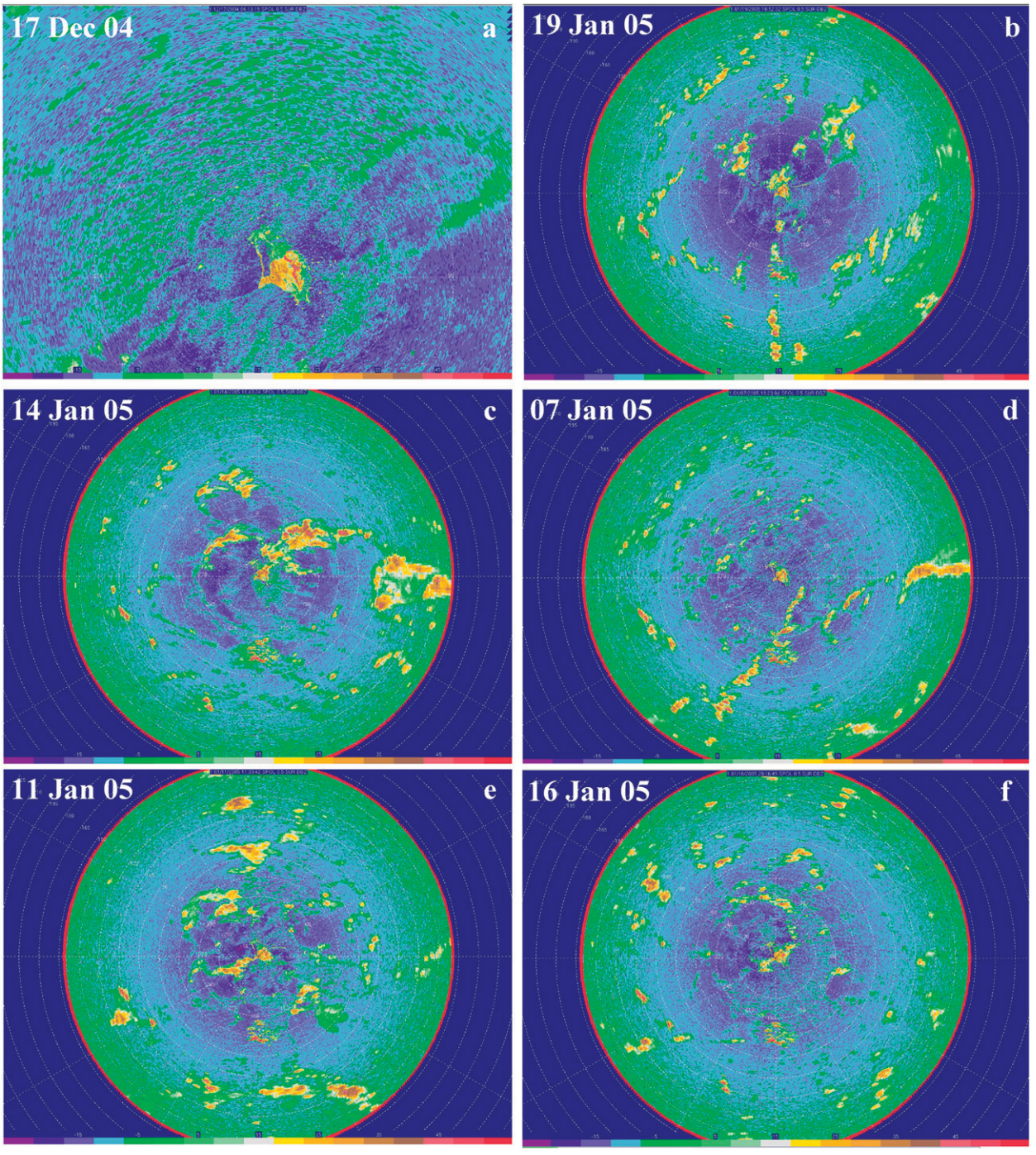

FIG. 19. Examples of PPIs showing the radar reflectivity factor and mesoscale cloud organization for each of the six analysis days: (a) 17 Dec 2004, (b) 19 Jan 2005, (c) 14 Jan 2005, (d) 7 Jan 2005, (e) 11 Jan 2005, and (f) 16 Jan 2005. Panel (a) is magnified so that the small clouds on the roll circulations can be seen.

APPENDIX

Cloud Positions

TABLE A1. Location of all clouds used in the analysis.

Cloud	Date	Time (UTC)	Range (m)	Azimuth (°)	Elev (°)
1	14 Jan 05	1453:32	26 531.6	29.5	4.5
2	14 Jan 05	1912:09	25 932.0	23.5	5.8
3	14 Jan 05	1914:59	22 034.7	1.0	3.5
4	14 Jan 05	1859:31	31 178.4	357.2	2.5
5	14 Jan 05	1915:26	24 732.9	346.8	4.5
6	14 Jan 05	1915:26	25 782.2	9.3	4.5
7	14 Jan 05	1938:50	46 617.7	50.0	2.5
8	14 Jan 05	1914:03	27 880.7	42.8	1.5
9	14 Jan 05	1903:16	34 326.2	7.6	2.5
10	14 Jan 05	1930:58	33 426.9	17.6	1.5
11	14 Jan 05	1945:52	45 268.7	55.8	1.5
12	14 Jan 05	1107:48	45 868.2	44.3	1.5
13	14 Jan 05	1946:20	25 482.4	41.5	2.5
14	14 Jan 05	1950:33	26 231.8	29.0	3.5
15	14 Jan 05	1946:48	25 932.0	26.5	4.5
16	14 Jan 05	1949:37	48 566.4	11.6	1.5
17	11 Jan 05	2021:42	34 176.3	333.4	2.5
18	11 Jan 05	1312:27	49 615.7	3.5	1.5
19	11 Jan 05	1446:31	24 433.1	49.8	4.5
20	11 Jan 05	1207:46	43 769.7	336.7	2.5
21	11 Jan 05	1214:42	42 120.8	335.7	2.5
22	11 Jan 05	1243:34	41 071.6	350.3	2.5
23	17 Dec 04	1637:37	48 866.2	54.9	1.5
24	17 Dec 04	1626:35	34 326.2	51.2	2.0
25	17 Dec 04	752:29	17 837.7	20.2	4.5
26	17 Dec 04	832:19	24 133.3	306.7	2.5
27	17 Dec 04	836:24	33 576.8	293.8	1.5
28	17 Dec 04	2014:51	44 069.5	84.1	2.0
29	17 Dec 04	2117:56	29 229.8	118.0	2.8
30	17 Dec 04	740:19	21 285.3	29.1	3.5
31	19 Jan 05	1534:10	34 925.8	17.4	2.5
32	19 Jan 05	1010:57	44 219.4	34.3	1.5
33	19 Jan 05	1815:40	47 667.0	326.1	1.5
34	19 Jan 05	1307:22	37 923.7	18.5	1.5
35	19 Jan 05	1300:27	38 823.1	15.5	0.5
36	19 Jan 05	1922:07	50 215.2	328.0	0.5
37	19 Jan 05	1130:23	23 533.7	294.8	3.5
38	19 Jan 05	1352:55	41 970.9	28.0	1.5
39	19 Jan 05	1447:17	20 535.8	33.6	4.5
40	19 Jan 05	1350:04	32 077.8	25.1	2.5
41	7 Jan 05	1603:30	39 722.5	306.7	1.5
42	7 Jan 05	1553:40	46 317.9	11.4	2.5
43	7 Jan 05	1621:25	32 677.4	40.5	3.5
44	7 Jan 05	1610:20	50 365.1	53.8	1.5
45	7 Jan 05	1614:10	48 116.7	52.9	2.5
46	7 Jan 05	1553:15	48 266.6	26.7	1.5
47	7 Jan 05	1600:56	43 619.8	17.3	2.5
48	7 Jan 05	1553:15	30 279.0	286.7	1.5
49	7 Jan 05	1756:37	33 876.5	305.1	2.5
50	7 Jan 05	1817:56	25 032.7	353.6	4.5
51	7 Jan 05	2214:10	49 465.8	345.5	2.0
52	7 Jan 05	2221:51	42 270.7	342.8	1.2
53	7 Jan 05	2217:09	41 671.2	338.6	2.8
54	7 Jan 05	2200:53	41 521.3	341.2	1.3
55	7 Jan 05	2216:44	44 968.9	61.7	2.0
56	7 Jan 05	2224:01	43 469.9	309.7	1.3
57	7 Jan 05	2235:09	31 178.4	315.2	2.8
58	7 Jan 05	2240:17	49 915.4	16.6	2.0
59	7 Jan 05	2314:08	31 028.5	348.6	3.5
60	7 Jan 05	2331:43	29 529.6	342.1	2.8
61	7 Jan 05	2345:24	18 886.9	340.7	4.5
62	7 Jan 05	2340:16	24 583.0	329.8	4.5
63	16 Jan 05	1140:31	50 065.3	71.1	1.5
64	16 Jan 05	1328:18	42 870.3	48.7	1.5
65	16 Jan 05	1401:14	31 028.5	73.0	3.5
66	16 Jan 05	1321:47	50 814.8	56.6	2.5
67	16 Jan 05	1410:59	34 326.2	326.5	3.5
68	16 Jan 05	1401:38	34 326.2	326.5	3.5
69	16 Jan 05	1452:30	33 726.7	355.7	1.5
70	16 Jan 05	1508:47	46 617.7	16.4	1.5
71	16 Jan 05	1511:36	43 020.2	11.0	0.5
72	16 Jan 05	1625:33	25 782.2	352.0	3.5
73	16 Jan 05	1559:10	32 077.8	352.0	1.5
74	16 Jan 05	1728:52	35 825.2	346.5	2.5
75	16 Jan 05	1703:49	50 964.7	349.5	1.5
76	16 Jan 05	1716:52	48 416.5	2.7	1.5

REFERENCES

Albrecht, B. A., 1989: Aerosols, cloud microphysics, and fractional cloudiness. *Science,* **245,** 1227–1230.

Arthur, D. K., S. Lasher-Trapp, A. Abdel-Haleem, N. Klosterman, and D. S. Ebert, 2010: A new three-dimensional visualization system for combining aircraft and radar data and its application to RICO observations. *J. Atmos. Oceanic Technol.,* **27,** 811–828.

Battan, L. J., 1953: Observations on the formation and spread of precipitation in convective clouds. *J. Meteor.,* **10,** 311–324.

Betts, A. K., 1997: Trade cumulus: Observations and modeling. *The Physics and Parameterization of Moist Atmospheric Convection,* R. K. Smith, Ed., Kluwer Academic, 99–126.

Caylor, I. J., and A. J. Illingworth, 1987: Radar observations and modelling of warm rain initiation. *Quart. J. Roy. Meteor. Soc.,* **113,** 1171–1191.

Colón-Robles, M., R. M. Rauber, and J. B. Jensen, 2006: Influence of low-level wind speed on droplet spectra near cloud base in trade wind cumulus. *Geophys. Res. Lett.,* **33,** L20814, doi:10.1029/2006GL027487.

Feingold, G., H. Koren, H. Wang, H. Xue, and W. A. Brewer, 2010: Precipitation-generated oscillations in open cellular cloud fields. *Nature,* **466,** 849–852, doi:10.1038/nature09314.

Göke, S., H. T. Ochs III, and R. M. Rauber, 2007: Radar analysis of precipitation initiation in maritime versus continental clouds near the Florida coast: Inferences concerning the role of CCN and giant nuclei. *J. Atmos. Sci.,* **64,** 3695–3707.

Hudson, J. G., and S. Mishra, 2007: Relationships between CCN and cloud microphysics variations in clean maritime air. *Geophys. Res. Lett.,* **34,** L16804, doi:10.1029/2007GL030044.

Illingworth, A. J., 1988: The formation of rain in convective clouds. *Nature,* **336,** 754–756.

——, J. W. F. Goddard, and S. M. Cherry, 1987: Polarization radar studies of precipitation development in convective storms. *Quart. J. Roy. Meteor. Soc.,* **113,** 469–489.

Inman, R. L., 1969: Computation of temperature at the lifted condensation level. *J. Appl. Meteor.,* **8,** 155–158.

Johnson, D. B., 1979: The role of coalescence nuclei in warm rain initiation. Ph.D. thesis, University of Chicago, 119 pp. [NTIS-PB-298556/AS.]

——, 1982: The role of giant and ultragiant aerosol particles in warm rain initiation. *J. Atmos. Sci.,* **39,** 448–460.

——, 1993: The onset of effective coalescence growth in convective clouds. *Quart. J. Roy. Meteor. Soc.,* **119,** 925–933.

Knight, C. A., and L. J. Miller, 1993: First radar echoes from cumulus clouds. *Bull. Amer. Meteor. Soc.,* **74,** 179–188.

——, and ——, 1998: Early radar echoes from small, warm cumulus: Bragg and hydrometeor scattering. *J. Atmos. Sci.,* **55,** 2974–2992.

——, J. Vivekanandan, and S. G. Lasher-Trapp, 2002: First radar echoes and the early Z_{DR} history of Florida cumulus. *J. Atmos. Sci.,* **59,** 1454–1472.

——, L. J. Miller, and R. A. Rilling, 2008: Aspects of precipitation development in trade wind cumulus revealed by differential reflectivity at S band. *J. Atmos. Sci.,* **65,** 2563–2580.

Laird, N. F., H. T. Ochs III, R. M. Rauber, and L. J. Miller, 2000: Initial precipitation formation in warm Florida cumulus. *J. Atmos. Sci.,* **57,** 3740–3751.

Lasher-Trapp, S. G., C. A. Knight, and J. M. Straka, 2001: Early radar echoes from ultragiant aerosol in a cumulus congestus: Modeling and observations. *J. Atmos. Sci.,* **58,** 3545–3562.

Mielke, P. W., Jr., K. J. Berry, and G. W. Brier, 1981: Application of multi-response permutation procedures for examining seasonal changes in monthly mean sea-level pressure patterns. *Mon. Wea. Rev.,* **109,** 120–126.

Nuijens, L., B. Stevens, and A. P. Siebesma, 2009: The environment of precipitating shallow cumulus convection. *J. Atmos. Sci.,* **66,** 1962–1979.

Ochs, H. T., and R. G. Semonin, 1979: Sensitivity of a cloud microphysical model to a urban environment. *J. Appl. Meteor.,* **18,** 1118–1129.

Paluch, I. R., and C. A. Knight, 1986: Does mixing promote cloud droplet growth? *J. Atmos. Sci.,* **43,** 1994–1998.

Pincus, R., and M. C. Baker, 1994: Effects of precipitation on the albedo susceptibility of clouds in the marine boundary layer. *Nature,* **372,** 250–252.

Rauber, R. M., and Coauthors, 2007: Rain in shallow cumulus over the ocean—The RICO campaign. *Bull. Amer. Meteor. Soc.,* **88,** 1912–1928.

Reiche, C. K. H., and S. G. Lasher-Trapp, 2010: The minor importance of giant aerosol to precipitation development within small trade wind cumuli observed during RICO. *Atmos. Res.,* **95,** 386–399.

Siebesma, A. P., 1998: Shallow cumulus convection. *Buoyant Convection in Geophysical Flows,* E. J. Plate et al., Eds., Kluwer Academic, 441–486.

Snodgrass, E. R., L. Di Girolamo, and R. M. Rauber, 2009: Precipitation characteristics of trade wind clouds during RICO derived from radar, satellite, and aircraft measurements. *J. Appl. Meteor. Climatol.,* **48,** 464–483.

Stevens, B., 2005: Atmospheric moist convection. *Annu. Rev. Earth Planet. Sci.,* **33,** 605–643.

Szumowski, M. J., R. M. Rauber, and H. T. Ochs III, 1999: The microphysical structure and evolution of Hawaiian rainband clouds. Part III: A test of the ultragiant nuclei hypothesis. *J. Atmos. Sci.,* **56,** 1980–2003.

Twomey, S., 1974: Pollution and the planetary albedo. *Atmos. Environ.,* **8,** 1251–1256.

Woodcock, A. H., 1953: Salt nuclei in marine air as a function of altitude and wind force. *J. Meteor.,* **10,** 362–371.

——, and M. M. Gifford, 1949: Sampling atmospheric sea salt nuclei over the ocean. *J. Mar. Res.,* **8,** 177–197.

——, R. A. Duce, and J. L. Moyers, 1971: Salt particles and raindrops in Hawaii. *J. Atmos. Sci.,* **28,** 1252–1257.

Xue, H., G. Feingold, and B. Stevens, 2008: Aerosol effects on clouds, precipitation, and the organization of shallow cumulus convection. *J. Atmos. Sci.,* **65,** 392–406.